Gondwana Research 134 (2024) 347–364

Contents lists available at ScienceDirect

Gondwana Research

journal homepage: www.elsevier.com/locate/gr

Geochemical and temporal evolution of Indian MORB mantle revealed by the Investigator Ridge in the NE Indian Ocean

Antje Dürkefälden [a], Folkmar Hauff [a,*], Kaj Hoernle [a,b], Maxim Portnyagin [a], Jo-Anne Wartho [a], Dieter Garbe-Schönberg [b], Andrey Gurenko [c], Paul van den Bogaard [a], Andrea Kipf [a], Marcus Gutjahr [a]

[a] GEOMAR Helmholtz Centre for Ocean Research Kiel, Wischhofstraße 1-3, 24148 Kiel, Germany
[b] Institute of Geosciences, Kiel University, Ludewig-Meyn-Straße 10, 24118 Kiel, Germany
[c] Centre de Recherches Pétrographiques et Géochimiques (CRPG), UMR 7358, Université de Lorraine, 54501 Vandœuvre-lès-Nancy, France

ARTICLE INFO

Article history:
Received 29 September 2023
Revised 30 June 2024
Accepted 30 July 2024
Available online 2 August 2024
Handling editor: Sanghoon Kwon

Keywords:
Indian Mantle Domain
Geochemistry
Geochronology
Fracture zones
East Gondwana

ABSTRACT

The Investigator Ridge, located along the prominent Investigator Fracture Zone in the Wharton Basin, northeast Indian Ocean, was chosen to investigate the temporal and geochemical evolution of the Indian upper mantle. We present new $^{40}Ar/^{39}Ar$ age, as well as major and trace element and Sr-Nd-Pb-Hf isotope data, from a large part of this so far scarcely sampled ridge. The $^{40}Ar/^{39}Ar$ ages range from 100.0 Ma to 64.1 Ma, and except for the two youngest samples (65.5 and 64.1 Ma) of likely Christmas Island Seamount Province (CHRISP) origin, display decreasing ages along the ridge from south to north. This pattern is consistent with the ages derived from paleomagnetic anomalies on the local oceanic crust that also decrease in age northwards and suggests an origin of the studied rocks at or near the now extinct Wharton spreading center. These ages also provide information about the displacements along the multiple Investigator Fracture Zones indicating large left-lateral as well as right-lateral offsets of the paleo spreading axis. The fracture zone also shows signs of recent tectonic reactivation. The Investigator Ridge samples are derived from a DUPAL-like mantle source similar to present-day Indian MORB. This source contains a depleted mantle type component, an enriched, moderately HIMU-like, component such as common "C" or "FOZO", and an additional enriched component of recycled subcontinental lithospheric mantle material. In both the Investigator Ridge and CHRISP samples, the trace element and isotope compositions systematically change with age implying a temporal geochemical evolution of the Indian Mantle Domain in this region. It contained higher proportions of subcontinental lithospheric material delaminated during breakup of Gondwana and mixed with depleted upper mantle material in its early phase. With time, the source evolved in the direction of "C" or "FOZO", which then became the dominant enriched component and is observed in the youngest samples.

1. Introduction

Studies of mid-ocean ridge basalts (MORBs) reveal that the upper mantle beneath the Indian (and the South Atlantic) Ocean has compositions distinct from those beneath the Pacific and North Atlantic Oceans, namely that Indian MORB displays more enriched, DUPAL-like, isotopic compositions (e.g., Castillo, 1988; Dupré and Allègre, 1983; Storey et al., 1989). The so-called DUPAL anomaly (Hart, 1984) is a large enriched geochemical mantle domain stretching beneath the Indian Ocean and into the South Atlantic Ocean. It is characterized by anomalously high $^{87}Sr/^{86}Sr$ and low $^{143}Nd/^{144}Nd$ and $^{176}Hf/^{177}Hf$ isotope ratios, as well as high $^{207}Pb/^{204}Pb$ and $^{208}Pb/^{204}Pb$ isotope ratios for a given $^{206}Pb/^{204}Pb$ isotope ratio. The origin and evolution of this so-called Indian Mantle Domain is still controversial. The different proposed models include contamination of the Indian upper mantle by (1) altered oceanic crust and sediments or mantle wedge material through ancient subduction processes (e.g., Kempton et al., 2002; Rehkämper and Hofmann, 1997), (2) continental lithospheric material related to deep recycling through mantle plumes (Castillo, 1988; Storey et al., 1989; Wen, 2006) or (3) subcontinental lithospheric mantle (SCLM) and/or lower crust possibly delaminated during rifting and breakup of Gondwana (Escrig et al., 2004; Gautheron et al., 2015; Hanan et al., 2004; Hoernle et al., 2011a; Meyzen et al., 2005).

* Corresponding author.
E-mail address: fhauff@geomar.de (F. Hauff).

https://doi.org/10.1016/j.gr.2024.07.016
1342-937X/

Hoernle et al. (2011a) showed that shallow recycling of delaminated continental lithosphere at a mid-ocean ridge could have been involved in the generation of the Christmas Island Seamount Province (CHRISP), an E-W trending chain of seamounts within the Wharton Basin in the Eastern Indian Ocean. In this region, the oceanic lithosphere has been generated over the last ~ 160 Ma by spreading along the Central Indian Ridge (CIR), the Southeast Indian Ridge (SEIR) and the now extinct Wharton Spreading Center (WSC; e.g., Gibbons et al., 2013; Müller et al., 2019). It forms the Indo-Australian plate, which does not behave as a single rigid plate, but can be considered as a composite plate consisting of the Indian plate, the Australian plate and the Capricorn microplate along with several broad zones of diffuse deformation (e.g., Deplus et al., 1998; Royer and Gordon, 1997). In the north, the Indian subcontinent collided with Eurasia forming the Himalayas, whereas in the east, the oceanic lithosphere is still being subducted beneath Sumatra and Java along the Sunda Trench. There is evidence of currently active intraplate deformation in the equatorial Indian Ocean due to the high stresses in the oceanic lithosphere caused by the ongoing collision of India with Eurasia (e.g., Deplus, 2001; Deplus et al., 1998).

The Wharton Basin is dissected by a number of long N-S to NNW-SSE striking faults that run roughly parallel to the Ninetyeast Ridge located to the west. Liu et al. (1983) identified these faults as fracture zones (FZs) of the fossil WSC located to the north. The most prominent of these FZs is the complex Investigator FZ that also comprises the Investigator Ridge, a ~ 1800 km long and roughly N-S striking (between 98° and 99°E longitude) bathymetric high running along this FZ (Fig. 1). It extends from 18°S to about 2°S latitude, where it subducts beneath Sumatra, and it crosses the western part of the CHRISP. Based on magnetic data, the oceanic crust on both sides of the Investigator FZ is offset by about 800–900 km in a left-lateral sense, and thus younger crust in the west is adjacent to older crust in the east. So far, the Investigator Ridge has been only sparsely explored and the few published geochemical data mainly comprise major element data and only a few trace element and Sr-Nd-Pb isotope data from samples dredged on the southern part of the ridge and in the Wharton Basin to the west and east (Sushchevskaya et al., 1998, 2000). All published $^{40}Ar/^{39}Ar$ ages of Hoernle et al. (2011a) and Gibbons et al. (2012) have been recalculated for reasons outlined in Section 2.2. A single volcanic glass sample recovered at the southern termination of the Investigator Ridge has a recalculated age of 155.6 ± 3.4 Ma and is interpreted by Gibbons et al. (2012) to be part of a sliver of Jurassic seafloor embedded in Cretaceous seafloor. In comparison, a glass sample from an isolated seamount (Outsider Seamount) to the west of the northern part of the Investigator Ridge gave a considerably younger $^{40}Ar/^{39}Ar$ age (Hoernle et al., 2011a) that is now recalculated to 54.32 ± 0.32 Ma.

During R/V SONNE cruise SO199 in 2008, the Investigator Ridge was systematically mapped and sampled by dredging (Fig. 1). The SO199 cruise report including on board sampling procedures and macroscopic sample descriptions is provided open access (Werner et al., 2009), and photographs of representative rock samples are provided in Fig. 1 of Supplementary Data 1. This study presents new $^{40}Ar/^{39}Ar$ age dating, major and trace element as well as Sr-Nd-Hf and Pb double-spike (DS) isotope analyses on bulk volcanic and plutonic rocks along with comprehensive analyses of fresh volcanic glass including CO_2, H_2O, F, S and Cl. Our overall motivation is to gain new insights into the tectonic, geochemical and temporal evolution of the oceanic crust in this part of the Indian Ocean during the Cretaceous and Paleocene, to investigate how far back the DUPAL signature can be traced in the Indian MORB and if its composition has changed with time, thereby contributing to a better understanding of the temporal evolution of the Indian Mantle Domain.

2. Analytical methods

2.1. Sample preparation

On board the R/V SONNE, Mn crusts and alteration halos were cut off using a rock saw to yield the freshest parts of the samples. In onshore laboratories, these rock slabs were crushed into small pieces using a jaw crusher, repeatedly cleaned with deionized water in an ultrasonic bath and dried in an oven at 50 °C. In order to select the least altered material and to best possible avoid alteration phases in vesicles and veins, the 0.5 to 2 mm sized rock chips were carefully hand-picked under a binocular microscope. Sample powders for major and trace element and Hf isotope analyses were prepared from a subset of these rock chips using an agate mortar grinder and an agate swing mill. The rims of rock samples that contained fresh glass and one hyaloclastite were carefully crushed in a mortar, then washed and dried as described above, and the freshest glass chips were hand-picked. For major and trace element analyses, the glass chips were embedded in a mount using a two-component epoxy resin-based adhesive. For $^{40}Ar/^{39}Ar$ age dating, plagioclase, amphibole and basalt matrix separates were hand-picked under a binocular microscope and the plagioclase separates were treated with 5 % hydrofluoric acid for 10 min. All samples were then cleaned in distilled water using an ultrasonic disintegrator.

2.2. $^{40}Ar/^{39}Ar$ age dating

All published $^{40}Ar/^{39}Ar$ ages (Hoernle et al. 2011a, Gibbons et al. 2012) have been recalculated using the decay constants of Steiger & Jäger (1977) and the flux monitor ages of Fleck et al. (2019) to be consistent with our new $^{40}Ar/^{39}Ar$ ages, and all sample ages are quoted with 2σ errors, unless otherwise stated. The new ages presented here are based on five plagioclase, two amphibole and one basalt matrix separates from six samples using the $^{40}Ar/^{39}Ar$ laser step-heating technique employed at the Argon Geochronology in Oceanography (ArGO) Laboratory at GEOMAR Helmholtz Centre for Ocean Research Kiel, Germany. A detailed description of the analytical methods can be found in Samrock et al. (2019). The samples were irradiated in Cd-shielded irradiation cannister #32 in March 2009, in the C6 position of the GKSS Research Centre (Geesthacht, Germany) nuclear reactor, at 5 MW for 168 h. The fast neutron flux was monitored using Taylor Creek Rhyolite sanidine (TCR-2 with an age of 28.344 ± 0.011 Ma; 1σ; Fleck et al., 2019).

The samples were step-heated using a Spectra Physics 25 W laser (455–515 nm). Argon isotopes were measured using a Mass Analyser Products 216 mass spectrometer, with an electron multiplier sensitivity of 2.70 x 10^{-10} cm^3/V (1.203 x 10^{-14} mol/V) at a trap current of 240 μA. The $^{40}Ar/^{39}Ar$ ages were calculated using the ^{40}K decay constants, $^{40}K/K$ ratio and $^{40}Ar/^{36}Ar$ atmospheric ratio of Steiger and Jäger (1977). The plateau and weighted mean ages, age spectra, and inverse isochron ages and plots were produced using the Isoplot program (v. 4.15) developed by Ludwig (2011). The nuclear interference reaction correction factors were $^{39}Ar/^{37}Ar_{Ca}$ = 9.44 x 10^{-4}, $^{36}Ar/^{37}Ar_{Ca}$ = 4.41 x 10^{-4}, and $^{40}Ar/^{39}Ar_K$ = 6.00 x 10^{-3}. The inverse isochron Spreading Factors (SF) were calculated after Jourdan et al. (2009). The $^{36}Ar/^{39}Ar$ and $^{36}Ar/^{37}Ar$ Alteration Index (AI) values were calculated after Baksi (2007), using the AI cut-off values recommended by Baksi (2007) and van den Bogaard (2013). Combined $^{40}Ar^*/^{39}Ar$ ages on multiple splits were calculated after Heath et al. (2018). Errors on the plateau, pseudo-plateau and weighted mean ages are quoted at 2σ, and all inverse isochron and combined $^{40}Ar^*/^{39}Ar$ age errors are quoted at 95 % confidence (95 % conf.). An expanded summary

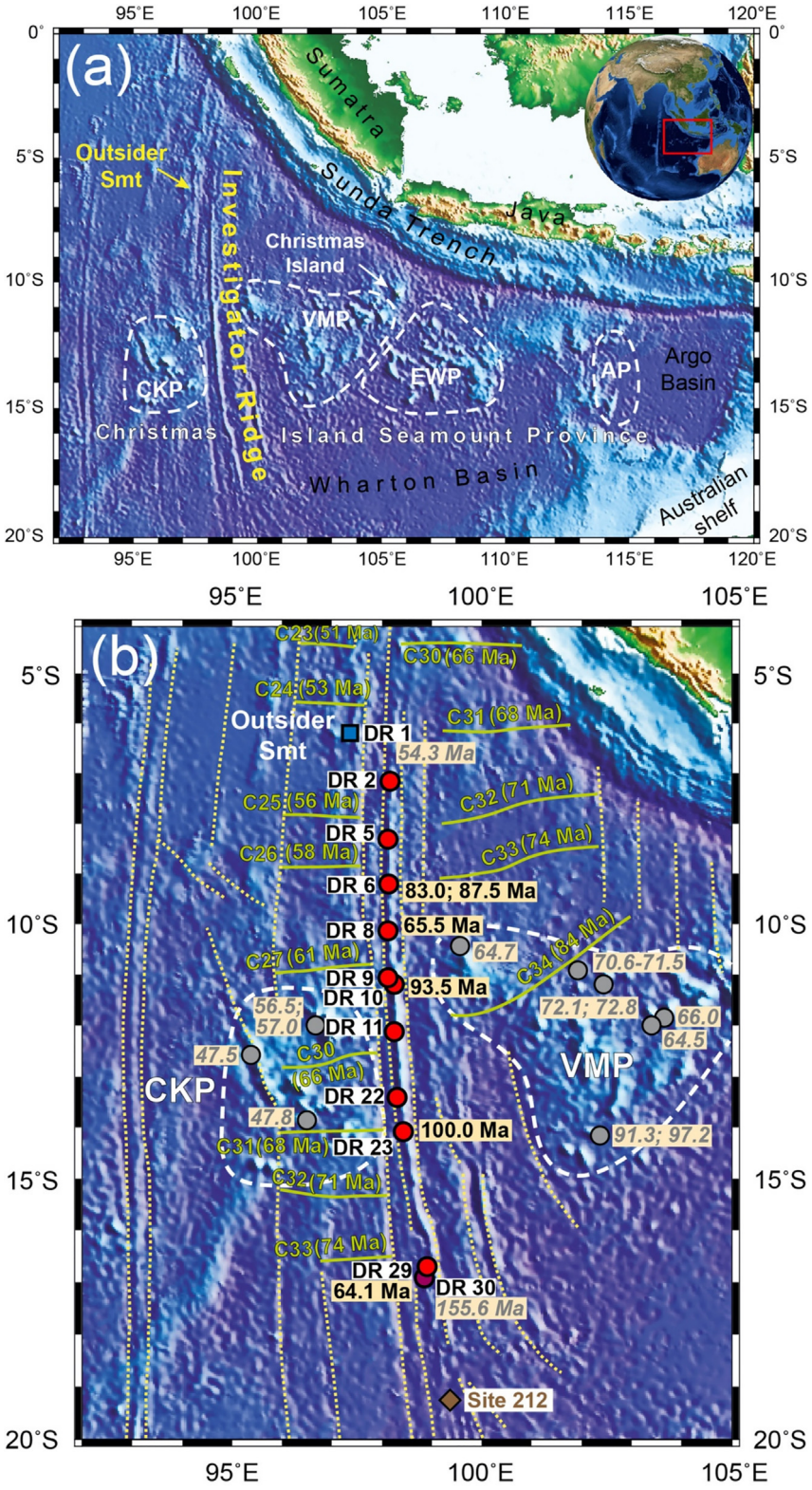

Fig. 1. Geologic setting of the Investigator Ridge (a) The red box within the inset globe shows the approximate location of the SO199 working area in the northeastern Indian Ocean. The overview map of the Wharton Basin includes the Investigator Ridge and Fracture Zone and the CHRISP crossing the ridge. The CHRISP is subdivided into different volcanic provinces (white dashed lines) with AP=Argo Basin Province, EWP=Eastern Wharton Province, VMP=Vening-Meinesz Province and CKP=Cocos-Keeling Province. (b) Map of the Investigator Ridge showing the dredge locations of the analyzed samples (red circles), including $^{40}Ar/^{39}Ar$ ages from this study (black ages in Ma). The recalculated literature $^{40}Ar/^{39}Ar$ ages (gray italic ages in Ma) for a sample from the Outsider Seamount (blue square) and for samples from the CKP and the younger VMP (gray circles) are from Hoernle et al. (2011a) and for a sample from dredge DR30 (dark red circle) from Gibbons et al. (2012). The location of DSDP Leg 22 Site 212 (brown diamond) is also shown (von der Borch et al., 1974). Magnetic lineations (green lines) are from Jacob et al. (2014), with corresponding chron ages in green using the time scale of Seton et al. (2012). Yellow dotted lines mark fracture zones identified by Jacob et al. (2014).

table and individual sample ^{40}Ar-^{39}Ar data and plots are shown in Supplementary Data 2.

2.3. Major elements

Major element analyses of whole rock samples were performed on fused beads using a Phillips X'Unique PW1480 X-ray fluorescence spectrometer (XRF) at GEOMAR equipped with a Rh-tube, and H_2O and CO_2 were analyzed by an infrared photometer (Rosemount CSA 5003). A subset of samples was analyzed at the Acme Analytical Laboratories Ltd. (AcmeLabs) in Vancouver, Canada, by ICP-OES using a lithium metaborate/tetraborate fusion technique. The JB-2, JB-3, JA-2 and JR-1 standards were measured along with the samples on the GEOMAR XRF and the BIR-1, BHVO-2, BCR-2 and AGV- 2 standards as well as the Acme in-house standard SO18 at AcmeLabs (Supplementary Data 3; QC Table 1). The accuracy lies within 3 % of the reference values from Govindaraju (1994) and Jochum et al. (2005, 2016) for most of the elements and the reproducibility is typically better than 2 %.

Major element compositions of the glass samples were measured using a JEOL JXA 8200 Electron Microprobe (EMP) at GEOMAR and for each sample, 8 spots were analyzed in 4–6 different glass chips. For all measurements, the analytical conditions were 15 kV accelerating voltage, 6 nA current and 5 μm electron beam size and details of the analytical procedure, the standards used and data on long-term reproducibility of reference materials are reported by Portnyagin et al. (2020). Although the analytical technique used was developed for the analysis of hydrous rhyolite glasses, it was also found to give reliable results for basaltic glasses, e.g., as shown by analyses of USNM 111240/52 VG-2 glass (Jarosewich et al., 1980) analyzed as an unknown in one series with our samples (Supplementary Data 3; QC Table 2).

2.4. Trace elements

Trace element concentrations in whole rock samples were measured by inductively coupled plasma mass spectrometry (ICP-MS) on an Agilent 7500cs at the Institute of Geosciences, Kiel University, Germany, following the methods of Garbe-Schönberg (1993). In addition, some samples were analyzed at AcmeLabs by ICP-MS, using a lithium metaborate/tetraborate fusion technique. International rock standards BIR-1, BHVO-2, BCR-2, AGV-2 and the Acme in-house standard SO18 were prepared along with the samples and the accuracy is 4 % for most elements relative to the reference values from Jochum et al. (2016) (Supplementary Data 3; QC Tables 3 to 6). The reproducibility of sample replicates and the instrument stability monitored by running multiple analyses of the same sample digest over the course of an analytical session is typically better than 3 % (Supplementary Data 3, QC Tables 7 and 8).

For the determination of trace element concentrations in fresh glass samples, laser ablation (LA-)ICP-MS at the Institute of Geosciences, Kiel University, was utilized. The analyses were conducted using a QP-ICP-MS Agilent 7900 and a Coherent GeoLas ArF 193 nm Excimer HD LA system operated with a fluence of 5 J cm^{-2}, at a repetition rate of 10 Hz, using 60 μm diameter ablation craters. The ICP-MS was operated under standard conditions at 1500 W and was optimized for low oxide formation (typically ThO/Th $\leq$ 0.4 %). A large volume ablation cell modified for rapid wash-out (Fricker et al., 2011) with a flow rate of 0.7 l min^{-1} He and additional H_2 (14 ml min^{-1}) was used. Prior to introduction into the ICP-MS, the carrier gas was mixed with Ar ($\sim$1 l min^{-1}). Analyses of ten major elements (Si, Ti, Al, Fe, Mn, Mg, Ca, Na, K, P) and 46 trace elements were carried out and included 20 s background (laser-off) and 40 s signal (laser-on) measurements. Dwell times for different isotopes varied from 5 to 20 ms depending on their abundance and one complete measurement cycle had a duration of 0.883 ms. The calibration was based on SRM-NIST612 glass standard (Jochum et al., 2011) and matrix-corrected using KL2-G glasses (Jochum et al., 2006). The reference glasses BCR-2G and GOR132-G were measured as unknown samples in one series along with the SO199 glasses (Supplementary Data 3; QC Table 9). Initial data reduction was performed using Glitter software (Griffin et al., 2008), which includes manual selection of integration windows and preliminary calibration. The intensities were corrected for background, averaged over the selected intervals, normalized to the intensity of ^{43}Ca isotope and converted to concentrations (μg/g $\simeq$ ppm) by matching the sum of major element oxides to 100 wt.% (e.g., Pettke et al., 2004).

2.5. Volatiles

The analyses of CO_2, H_2O, Cl, F and S contents in volcanic glasses were conducted using a CAMECA IMS 1280 HR ion microprobe at the Centre de Recherches Pétrographiques et Géochimiques (CRPG) in Nancy, France. Glass chips previously analyzed for major elements by EMP were carefully re-polished to remove residual carbon coating, with final polishing using 0.25 μm Al_2O_3 suspension. The grains were then removed from the epoxy resin, remounted by pressing them into indium metal, ultrasonically cleaned and dried / stored at + 60 °C. About 12 to 24 h prior to analysis, the mount was placed into the sample chamber of the ion probe at $\sim 10^{-8}$ Torr pressure. A liquid nitrogen cold trap and a sublimation pump were always used to reduce CO_2 and H_2O background and maintain a pressure of $< 2 \times 10^{-9}$ Torr in the sample chamber. Prior to each measurement, the samples were pre-sputtered for 300 s with a 0.3–0.4 nA, 10 kV $^{133}Cs^+$ primary beam focused to < 5 μm spot and rasterized over a 20 × 20 μm area; the raster was then reduced to 10 × 10 μm during analyses. A field aperture of $\sim$ 1000 μm and 80 % e-Gate were used to eliminate any secondary ion signal from the spot margins. A mass-resolving power of $\sim$ 5000 was applied, enough to resolve ^{17}O from ^{16}OH and ^{29}SiH from ^{30}Si peaks. The $^{12}C^-$ (counting time 8 s), $^{16}OH^-$ (6 s), $^{19}F^-$ (6 s), $^{27}Al^-$ (2 s) and $^{30}Si^-$ (2 s), $^{32}S^-$ (4 s) and $^{35}Cl^-$ (6 s) ions were counted for 12 cycles, using an axial electron multiplier. A set of reference glasses (ALV981-R23, 30–2, 40–2, VG2 USNM111240, CY82-29–3 V, CLDR01-5 V, KL2-G, Etna-II-6 and Etna-II-7; see Sobolev et al. (2016) for their accepted compositions) and San Carlos olivine were analyzed to create calibration lines, which were then used to determine the volatile concentrations in the unknown samples. Based on the established calibration lines, the accuracy of Secondary Ion Mass Spectrometry (SIMS) analyses, calculated as average relative deviation of the measured values from the reference ones, was estimated to be $\leq$ 15 % for CO_2 and $\leq$ 10 % for H_2O, F, S and Cl (95 % confidence level). Background values calculated assuming negligible (zero) contents of the volatiles in glass KL2-G were 24–35 μg/g for CO_2, 140 μg/g for H_2O, and in olivine 6–7 μg/g for F, 0.6–1.1 μg/g for S and 0.8–1.5 μg/g for Cl. Every sample was analyzed using three spots.

2.6. Sr-Nd-Pb-Hf radiogenic isotope ratios

Sr-Nd-Pb-Hf isotope analyses of whole rock chips and powders from the Investigator Ridge were processed at GEOMAR from 2008 to 2011 along with samples from the CHRISP using the same analytical procedures as described in Hoernle et al. (2011a). Additional analyses of glass chips were conducted at GEOMAR in 2021–2022 using a Thermo Scientific TRITON Plus thermal ionization mass spectrometer (TIMS) for Sr, Nd and Pb, and a NEPTUNE Plus MC-ICP-MS for Hf. Sr-Nd and Pb-Hf were collected in multi-dynamic and static collector modes, respectively. About 200 mg of fresh

glass chips were leached in 2 N HCl at 50 °C for 30 min and then triple rinsed in 18.2 MΩ water prior to digestion. Sample dissolution and Sr-Nd-Pb element chromatography followed established standard procedures (Hoernle et al., 2008) with a modified Sr clean-up using Sr-Spec microcolumns. Hf was separated using a cation exchange column (AG50W-X8, 100–200 mesh) over the first 2 ml using a 1.5 M HCl media, followed by a Hf clean-up using 0.2 ml of TODGA resin (50–100 μm; DN-B10-S TRISKEM®) after Connelly et al. (2006). Total chemistry blanks were <100 pg for Sr, <50 pg for Nd, Hf and <30 pg for Pb and thus are all considered negligible relative to the amount of sample processed. Sr and Nd isotope ratios were mass-bias corrected within each run to $^{86}Sr/^{88}Sr$ = 0.1194 and $^{146}Nd/^{144}Nd$ = 0.7219, respectively. Reference materials were analyzed along with the samples and produced an average $^{87}Sr/^{86}Sr$ value of 0.710250 ± 0.000009 (2 standard deviation (2SD); n = 8) for NBS987, and a $^{143}Nd/^{144}Nd$ average value of 0.511850 ± 0.000006 (2SD; n = 7) for La Jolla. Pb isotope ratios were determined using the Pb double-spike (DS) technique described in Hoernle et al. (2011b) for mass-bias correction. Long term DS-corrected average values for NBS981 are $^{206}Pb/^{204}Pb$ = 16.9408 ± 0.0019, $^{207}Pb/^{204}Pb$ = 15.4974 ± 0.001 9 and $^{208}Pb/^{204}Pb$ = 36.7206 ± 0.0050 (2SD; n = 228) since installation of the instrument in 2014. Our in-house SPEX CertiPrep® Hf ICP standard solution (lot #9) gave $^{176}Hf/^{177}Hf$ = 0.282170 ± 0.00 0005 (2SD; n = 36), corresponding to $^{176}Hf/^{177}Hf$ = 0.282163 for JMC475. Results of acid leached USGS reference material BCR-2 processed along with the samples are shown in Supplementary Data 3 (QC Table 10), and agree well with the values of Fourny et al. (2016) and Todd et al. (2015). Replicate analysis by means of a second sample digestion was carried out for volcanic sample SO199-DR9-1 (Hf only) and plutonic sample SO199-DR23-14 (Sr-Nd-Pb-Hf). While $^{176}Hf/^{177}Hf$ reproduced within 2SE, somewhat larger offsets outside the 2SD uncertainties are observed for radiogenic Sr, Nd and Pb isotope ratios of the replicated plutonic sample DR23-14. This is attributed to the use of rock chips for Sr-Nd-Pb chemistry, which in case of plutonic rocks introduces compositional heterogeneities through variations in the mineral assemblage processed. Hf chemistry was carried out on powders that apparently levels out any such heterogeneities. Nevertheless, due to the generally low Pb contents in these mid-ocean ridge igneous rocks (≪1 μg/g), we preferred to process rock chips, since external Pb is potentially added by the powder milling.

3. Results

3.1. Bathymetric mapping

During cruise SO199, the Investigator Ridge was almost fully mapped over ~ 1,300 km between 6°S and 18°S using a Kongsberg SIMRAD EM 120 multi-beam echo sounder. The ridge rises ~ 600 m in the north to ~ 2800 m in the central part above the surrounding seafloor and varies in width between ~ 10–25 km. In the northern part, the structure consists of two parallel ridges separated by a valley (Fig. 2a). To the south, the western ridge becomes more diffuse and disappears in the central and southern section of the Investigator Ridge, whereas the eastern ridge becomes more prominent, especially in the central section (Fig. 2b and c). Along almost its entire mapped length, the eastern ridge is marked by an asymmetrical structure with a steep west-facing scarp and a gentle eastern slope. Between ca. 10°55′S and 11°20′S in the central part of the Investigator Ridge, the ridge crest is offset ~ 10 km to the east and broadens (Fig. 2b). In this offset area, the contour lines strike in an unusual E-W direction and then bend into the prevailing N-S direction, which may indicate the existence of a E-W oriented fossil spreading center on the eastern side of the Investigator Ridge. Approximately 10–20 km west of the southern part of the Investigator Ridge between ~ 16°30′S and 17°S, several ridge- and plateau-like structures rise ~ 1000 m above the surrounding seafloor and are separated from the main ridge and from each other by canyons (Fig. 2c; Werner et al., 2009).

The Outsider Seamount, an isolated seamount located about 80 km to the west of the northern part of the Investigator Ridge at ~ 6°15′S, was also mapped (Fig. 2d). It rises more than 2,300 m above the surrounding seafloor and is oval-shaped. Its southern and, less pronounced, northern flank are crossed by a N-S oriented ravine and the eastern half of the seamount top appears to be offset to the north by ~ 1 km relative to the western half, suggesting left-lateral displacement along a N-S striking fault zone cutting the middle and upper slopes of the seamount after its emplacement (Werner et al., 2009).

3.2. $^{40}Ar/^{39}Ar$ age dating results

One basalt matrix (DR6-2) and three plagioclase samples (DR8-5, 23–14 (split 1) and 29–1) yielded plateau or pseudo-plateau ages with concordant inverse isochron ages. The remaining two amphiboles (DR6-6 and 10–2) and three plagioclases (DR10-2 and 23–14 (split 2)) gave medium- and high-temperature weighted mean ages (WMA). All the samples displayed slightly disturbed to very disturbed L-, U-, staircase or hump-shaped age spectra and were highly affected by alteration. All but one step yielded $^{36}Ar/^{39}Ar$ or $^{37}Ar/^{39}Ar$ Alteration Index values above the cut-off values (Supplementary Data 2). A summary of the $^{40}Ar/^{39}Ar$ data is shown in Table S1.

Basalt matrix sample DR6-2 yielded a disturbed L-shaped age spectrum, with a plateau age of 83.0 ± 1.8 Ma (Mean Square Weighted Deviation (MSWD) = 0.98; Probability (P) = 46 %) from 63.4 % of the total ^{39}Ar (steps 9–20). The inverse isochron age of 78.6 ± 8.7 Ma (MSWD=0.97, P=47 %; initial $^{40}Ar/^{36}Ar$ = 297.6 ± 4.0) was concordant with the plateau age, but yielded a low Spreading Factor (SF) value of 7.1 % below the accepted threshold of 40 %. Steps 1–6 were measured using an uncalibrated lower gain setting on the electron-multiplier detector resistor and therefore were not used in age determinations.

Amphibole sample DR6-6 gave a disturbed U-shaped age spectrum, with a medium-temperature WMA of 87.5 ± 1.9 Ma (MSWD = 1.6, P = 20 %) from 32.7 % of the total ^{39}Ar (steps 4–5). No inverse isochron was obtainable from the 2 WMA steps, but inverse isochron ages from adjacent steps (85.6 ± 1.6 and 87.8 ± 6. 5 Ma from steps 1–4 and 7–14, respectively) yielded ages that were concordant with the medium-temperature WMA. Steps 1–4 and 7–14 showed evidence of excess ^{40}Ar yielding initial $^{40}Ar/^{36}Ar$ ratios of 302.8 ± 1.6 (MSWD = 2.5, P = 7.9 %, SF = 34.6 %) and 306.8 ± 7.7 (MSWD = 0.86, P = 52 %, SF = 27.0 %), respectively.

Plagioclase sample DR8-5 yielded a slightly disturbed L-shaped age spectrum, showing a plateau age of 65.5 ± 3.5 Ma (MSWD=1.3, P=28 %) from 63.9 % of the total ^{39}Ar (steps 5–13). The inverse isochron age of 72.5 ± 9.2 Ma (MSWD=0.88, P=50 %) was concordant with the plateau age, but the low SF value of 17.6 % and the poorly-constrained initial $^{40}Ar/^{36}Ar$ ratio of 278 ± 17 may suggest tight-clustering of the analyses or possible mass fractionation effects. The medium-temperature plateau age was obtained from altered material, therefore it may be a minimum age.

Amphibole and plagioclase splits from sample DR10-2 yielded concordant higher- and high-temperature WM ages of 92.6 ± 3.6 Ma (MSWD = 0.86, P = 46 %, 14.4 % ^{39}Ar, steps 10–13) and 94.0 ± 2.7 Ma (MSWD=1.2, P=29 %, 26.2 % ^{39}Ar, steps 13–19). Both splits gave disturbed age spectra, with a multiple hump-shape (amphibole) and L-shaped spectra (plagioclase). The amphibole split yielded a tightly-clustered inverse isochron age of 86 ± 27 Ma (MSWD=1.0, P=37 %, initial $^{40}Ar/^{36}$ = 335 ± 110) with

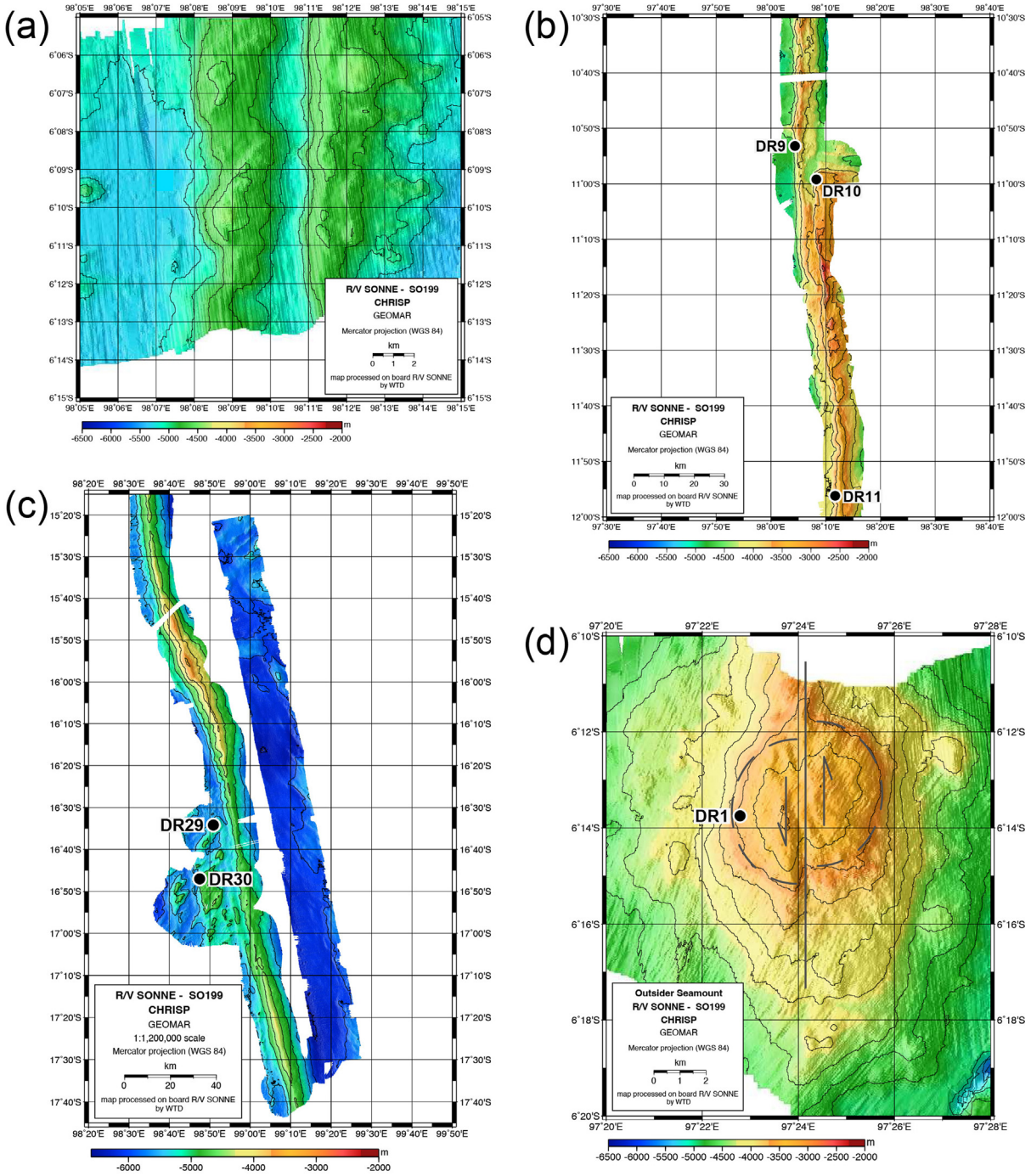

Fig. 2. Bathymetric maps of (a)-(c) selected segments of the Investigator Ridge and the (d) Outsider Seamount. Whereas the Investigator Ridge is divided into two parallel ridges in its northern section (a), the eastern ridge dominates in the central and southern sections and the western ridge has disappeared (b + c). The Outsider Seamount map (d) shows that the eastern half of the top of the seamount appears to be offset to the north relative to the western half indicating left-lateral movement after the formation of the seamount.

a low SF value of 13.1 % and the plagioclase split yielded no isochron due to clustering of the 7 steps near the radiogenic axis. A combined $^{40}Ar^*/^{39}Ar$ age of 93.5 ± 2.1 Ma (MSWD=1.0, P=41 %, *n* = 11 steps) from the 2 splits is the recommended age for this sample.

Two plagioclase splits from sample DR23-14 yielded concordant pseudo-plateau and high-temperature WM ages of 100.3 ± 2.5 Ma (MSWD=0.53, P=66 %, 48.3 % ^{39}Ar, steps 11–14) and 99.3 ± 3.5 Ma (MSWD=0.93, P=47 %, 26.5 % ^{39}Ar, steps 13–19). Split one gave a disturbed staircase age spectrum and split two yielded a slightly disturbed L-shaped age spectrum. Both splits yielded concordant but tightly-clustered inverse isochron ages of 100.6 ± 5.6 Ma (MSWD=0.79, P=45 %, initial $^{40}Ar/^{36}Ar$ = 295 ± 20, SF=30.0 %) and 96 ± 22 Ma (MSWD=1.1, P=37 %, initial $^{40}Ar/^{36}Ar$ = 314 ± 110, SF=14.3 %), respectively. A combined $^{40}Ar^*/^{39}Ar$ age of 100.0 ± 2.0 Ma (MSWD=0.74, P=69 %, *n* = 11 points) from the two splits is the recommended age for this sample.

Plagioclase sample DR29-1 yielded a disturbed staircase age spectrum showing a low-temperature plateau age of 64.1 ± 1.4 M a (MSWD=1.6, P=12 %) from 60.1 % of the total ^{39}Ar (steps 2–10).

The inverse isochron age of 64.2 ± 1.8 Ma (MSWD=1.8, P=7.8 %, SF=49.7 %, initial $^{40}Ar/^{36}Ar$ = 295.2 ± 3.9) is concordant with the plateau age. The low-temperature plateau age was obtained from altered material, therefore it may be a minimum age. An additional 19 samples and splits were also $^{40}Ar/^{39}Ar$ dated, but they failed to yield meaningful ages.

3.3. Geochemical results

For this study, we analyzed 20 volcanic and plutonic rocks from 9 different dredge sites along the Investigator Ridge and two volcanic rocks from a single site at the Outsider Seamount for whole rock major and trace elements, and a subset of 14 of these samples for Sr-Nd-Pb-Hf isotope ratios. Moreover, we report 13 major and trace element and six Sr-Nd-Pb-Hf isotope analyses of fresh glass from pillow margins and one hyaloclastite sample from five sites located at the Investigator Ridge and one site at the Outsider Seamount. Most of the collected igneous rock samples are fresh to slightly altered and only a few samples are moderately to strongly altered. The rocks are coated by thin (up to 1 mm) Fe-Mn crusts that were removed with a rock saw.

3.3.1. Major and trace elements

Major element data are reported in Table S2 and S3 and trace element data are reported in Table S4 and S5. The majority of the whole rock samples have loss on ignition (LOI) values ranging from 0.9 to 3.9 g/100 g and only a few samples show LOI values > 4 g/100 g. Relatively good correlations of MgO, CaO, FeOt and to a lesser extent Na_2O with immobile elements such as Zr and TiO_2 indicate that most of the major element compositions of the whole rocks are not significantly affected by seawater alteration. Regarding the use of trace elements to elucidate rock petrogenesis, we exclude the mobile elements Rb, U and Sr from the whole rock data and use the rare earth elements (REEs) and the high field strength elements (HFSEs), which are considered to be largely fluid-immobile during low temperature alteration processes. In contrast, the geochemical compositions of the fresh glass samples can be used without constraints, since they reflect pristine melt compositions.

Rock classification using the total alkali versus silica diagram (TAS, inset plot in Fig. 3a) after Le Bas et al. (1986) shows that the Investigator Ridge glasses are tholeiitic basalts and the glasses from the Outsider Seamount are transitional tholeiites along the alkaline-subalkaline division line of MacDonald and Katsura (1964). For the whole rocks, the Nb/Y versus Zr/Ti diagram after Pearce (1996) basically confirms this subdivision into basalts/gabbros for most Investigator Ridge samples, but samples DR8-1, DR8-5 and DR9-1 plot towards and within the alkali basalt field. As expected, the lavas from the Outsider Seamount lie on the separation line between the basalt and alkali basalt fields (Fig. 2 of Supplementary Data 1). On the Nb/Yb versus Th/Yb and Nb/Yb versus TiO_2/Yb diagrams after Pearce (2008), the Investigator Ridge and Outsider Seamount samples form a positive array ranging in composition from normal mid-ocean ridge basalt (N-MORB) through enriched (E-) MORB to ocean island basalt (OIB; Fig. 3a and b). Volcanic whole rock and glass samples from DR2, the northernmost dredge station on the Investigator Ridge, as well as sample DR6-2 further south and sample DR30-6 from a plateau-like structure west of the southernmost part of the Investigator Ridge are most depleted and compositionally similar to N-MORB. A number of moderately enriched volcanic rocks and glass samples from dredges DR5, DR10 and DR22, collected on the northern and central segment of the ridge, cluster in the vicinity of typical E-MORB compositions. Three basaltic samples recovered in the central part of the ridge (DR8-1, DR8-5 and DR9-1) show the most enriched compositions ranging from E-MORB to OIB signatures.

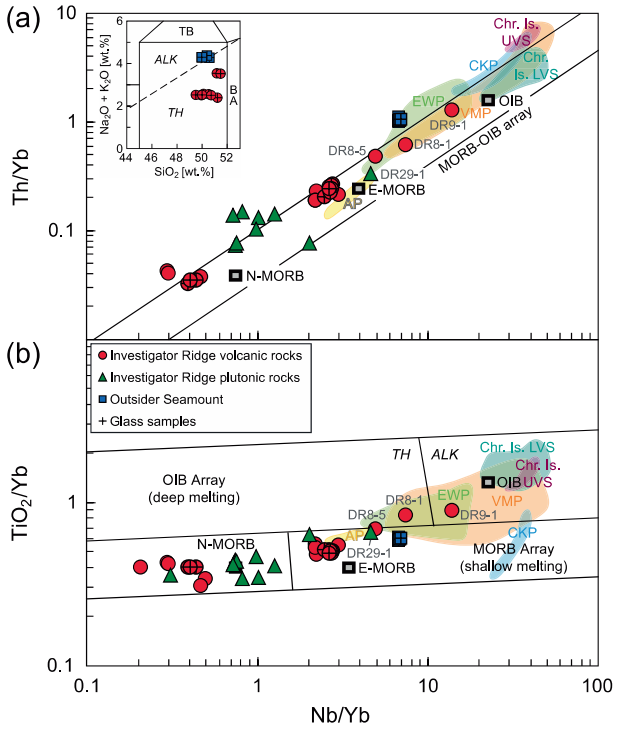

Fig. 3. Nb/Yb versus (a) Th/Yb and (b) TiO_2/Yb diagrams after Pearce (2008). The total alkali versus silica diagram, after Le Bas et al. (1986), is shown as an inset in (a) and classifies the glasses from the Investigator Ridge as tholeiites, whereas those from the Outsider Seamount are transitional tholeiites. Dashed line=alkaline/sub-alkaline division after MacDonald and Katsura (1964). TH=tholeiite, ALK=alkali basalt, BA=basaltic andesite and TB=trachybasalt. In (a) and (b), the whole rock and glass samples from the Investigator Ridge and the Outsider Seamount range from N-MORB through E-MORB to OIB compositions forming a positive array. In contrast to the other samples, the three most enriched samples lie within or on the boundary of the OIB array of deep melting. Together with the Outsider Seamount samples, they overlap with the CHRISP samples displayed as fields for the different volcanic provinces including AP=Argo Basin Province, EWP=Eastern Wharton Basin Province, VMP=Vening-Meinesz Province, CKP=Cocos-Keeling Province and Chr. Is. LVS/UVS=Christmas Island Lower and Upper Volcanic Series. Data from the CHRISP are from Falloon et al. (2022), Taneja et al. (2016) and from this study. Analytical errors are smaller than the symbol size.

They lie within or on the boundary of the deep-melting OIB array on the Nb/Yb versus TiO_2/Yb diagram with the most enriched sample DR9-1 lying within the alkalic OIB field, whereas all other analyzed rocks fall within the shallow-melting MORB array (Fig. 3b). The plutonic rocks were collected at different dredge sites on the northern, central and southern ridge portions and display compositions ranging between N-MORB and E-MORB. Most of them plot between the most depleted and the moderately enriched volcanic samples and resemble N-MORB. Gabbroic sample DR29-1 from one of the ridge-like structures west of the southern segment has compositions similar to the enriched volcanic sample DR8-5. Some of the more depleted plutonic rocks plot above the MORB-OIB array on the Nb/Yb versus Th/Yb diagram (Fig. 3a) due to higher Th concentrations compared to the other plutonic rocks. Samples from the Outsider Seamount have enriched compositions plotting between E-MORB and OIB but are also shifted toward higher Th/Yb ratios. Together with the enriched samples from the Investigator Ridge, they overlap with the compositions of samples from the CHRISP. Complementary CHRISP major and trace element whole rock data can be found in Supplementary Data 4.

On multi-element diagrams normalized to primitive mantle values after Hofmann (1988) with whole rock (excluding the mobile elements Rb, U, K, Sr and P) and glass samples shown on separate diagrams (Fig. 4a and b), the patterns of the depleted

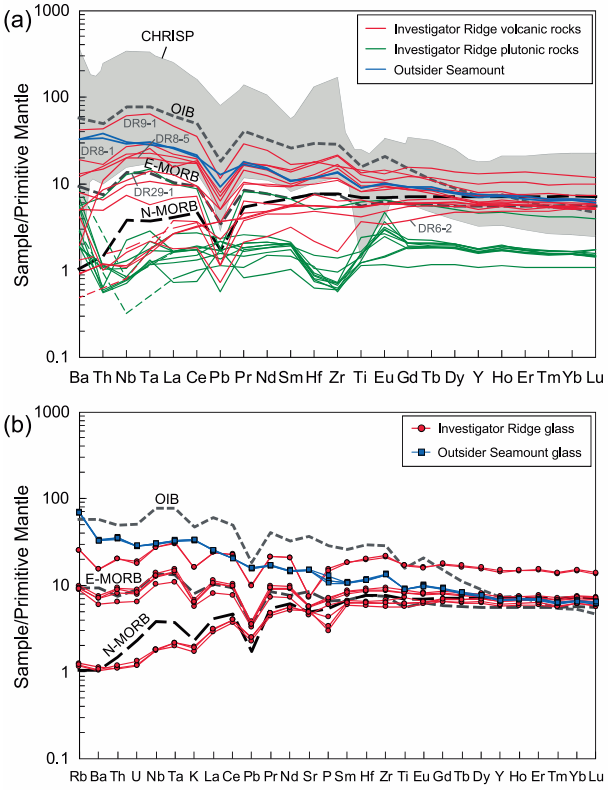

Fig. 4. Multi-element diagrams normalized to primitive mantle values after Hofmann (1988) for (a) whole rock samples (excluding the mobile elements) and (b) glass samples. The volcanic samples from the Investigator Ridge show element patterns ranging between the N-MORB and OIB patterns, but none of them show a depletion in HREEs typical for OIBs. The more enriched samples overlap with the CHRISP field (Falloon et al., 2022; Taneja et al., 2016 and this study). Except for DR29-1, the plutonic rocks have relatively flat shapes with generally much lower values relative to the volcanic rocks but with positive Ba and Eu and negative Hf and Zr anomalies. The patterns for the Outsider Seamount lie between those of E-MORB and OIB. The dashed lines in the element patterns are inferred due to concentrations below detection limits for Ta and Th (see also Table S4). Analytical errors are smaller than the symbol size.

samples are similar to average N-MORB with $(La/Sm)_N$=0.48–0.66, except that they have lower Nb, Ta and La values. The patterns of the moderately enriched samples are relatively flat, reflected by $(La/Sm)_N$ and $(Sm/Yb)_N$ values of 1.05–1.40 and 1.09–1.38, respectively, and they closely follow the E-MORB shape, although the patterns from DR6-6, DR10-16 and DR22 are overall shifted to higher values. The most enriched samples have outlines subparallel to that of OIB with $(La/Sm)_N$=1.77–2.78, but they are shifted to somewhat lower values. As their $(Sm/Yb)_N$ ratios are lower than 2.53, they do not show the strong depletion in HREEs that is typical for OIBs ($(Sm/Yb)_N \approx 5$), which would indicate melting in the presence of garnet.

The majority of the Investigator Ridge plutonic rocks yield relatively flat patterns with generally much lower incompatible element abundances relative to the volcanic rocks, but they show positive Eu and Ba anomalies and negative Hf and Zr anomalies indicating accumulation of plagioclase crystals. One exception is sample DR29-1 which is more similar to the E-MORB pattern (Fig. 4a). Sample DR6-2, although grouped with the volcanic samples, is somewhat exceptional, since it is a subvolcanic sample of doleritic texture and shows geochemical characteristics of both the volcanic and plutonic rocks. On the one hand, DR6-2 largely shows low incompatible element abundances, a positive Ba anomaly and a negative, albeit less pronounced, Hf-Zr anomaly, which is similar to the plutonic rocks. On the other hand, the pattern displays no positive Eu anomaly, the HREE abundances are higher than in the plutonic rocks and the HREE pattern resembles that of N-MORB and the depleted volcanic samples (Fig. 4a).

The patterns of the Outsider Seamount samples lie between the E-MORB and OIB patterns with $(La/Sm)_N$ values of 2.32–2.47 that are similar to OIB, but they have elevated Ba and Th values, and like the Investigator Ridge samples, they do not display OIB-typical HREE ($(Tb/Yb)_N$=2.14) depletion relative to the middle REEs with $(Tb/Yb)_N$=1.21–1.36.

3.3.2. Volatiles

The average volatile contents are reported in Table S6. H_2O contents in the Investigator Ridge glasses vary from 0.18 to 1.13 g/100 g and strongly correlate with K_2O (positively; R^2 = 0.99) and MgO (negatively; R^2 = 0.98). The glasses are characterized by relatively high H_2O/K_2O values of 2.0–3.2 and H_2O/Ce values of 258–312, with both ratios at the uppermost values for normal MORB (e.g., Dixon et al., 2002) and overlapping with compositions of plume-influenced MORB (Dixon et al., 2017) as well as with glasses from the Southwest Indian Ridge (Le Voyer et al., 2019; Wang et al., 2021). The trace element-enriched glasses from the Outsider Seamount have moderate H_2O contents of ~ 0.62 g/100 g and relatively low H_2O/K_2O values of 0.6 and H_2O/Ce values of 190, suggesting their origin from a relatively H_2O-depleted source.

CO_2 contents range from ~ 50 to 200 μg/g and together with low CO_2/Ba < 30 suggest significant degassing of the magmas prior to and during submarine eruption (e.g., Le Voyer et al., 2017). The maximum eruption depths estimated from the H_2O-CO_2 systematics using the VolatileCalc model of Newman and Lowenstern (2002) indicate eruption depths of ~ 1600 mbsl for the Outsider Seamount and 2400–4200 mbsl for the Investigator Ridge samples. These relatively deep-water eruptions are consistent with high S contents (see below).

The studied glasses have highly variable Cl contents from ~ 30 to ~ 750 μg/g and cover most of the MORB range (Kendrick et al., 2012; Michael and Schilling, 1989). Among the samples from the Investigator Ridge, low-K_2O glasses from station DR2 have the lowest Cl contents of ~ 38 μg/g and marginally mantle-like K/Cl values of ~ 13 and Cl/Nb values of ~ 35 (Kendrick et al., 2012; Le Voyer et al., 2015). Trace element-enriched samples DR10 and DR22 have the highest Cl contents of 460–745 μg/g, very low K/Cl values of ~ 3.1–5.6 and high Cl/Nb values of ~ 43–65 indicating significant assimilation of Cl-rich, K- and Nb-poor brine (Kendrick et al., 2012; Le Voyer et al., 2015). Trace element-enriched DR1 glasses from the Outsider Seamount have relatively low Cl contents of ~ 230 μg/g, the highest K/Cl value of ~ 38 and the lowest Cl/Nb value of ~ 12 which corresponds to mantle values and even more Cl-depleted compositions, such as a hypothetical highly Cl-depleted recycled crustal material (Kendrick et al., 2014; Stroncik and Haase, 2004).

Sulphur contents in the glasses range between ~ 950 and 2,000 μg/g and strongly correlate with FeO (positively; R^2 = 0.95) and MgO (negatively; R^2 = 0.98). The contents fall within the MORB FeO-S array, indicate saturation with an immiscible sulfide phase (Wallace and Carmichael, 1992) and no significant degassing (Wallace and Edmonds, 2011), which is consistent with the eruption depths of > 1500 mbsl estimated from the H_2O-CO_2 systematics.

3.3.3. Radiogenic isotopes

Seawater-rock interaction can significantly alter the Rb-Sr and U-Th-Pb isotope systems in submarine whole rocks, while the Sm-Nd and Lu-Hf schemes are considered inert. These secondary effects are therefore summarized in the following and their impact on the data set is evaluated before the results of the radiogenic isotope analyses are presented. $^{87}Sr/^{86}Sr$ in MORB type igneous rocks

is easily affected by seawater, as seawater contains ~ 7 μg/g Sr relative to MORB type rocks (100 ± 50 μg/g Sr) and has significantly more radiogenic $^{87}Sr/^{86}Sr$ compositions than MORB. $^{87}Sr/^{86}Sr$ in seawater evolved from ~ 0.707 to ~ 0.709 since the Mid-Cretaceous (Jones and Jenkyns, 2001). The tight cluster of volcanic samples (whole rock and glass) from the Investigator Ridge in the initial Sr-Nd isotope plot (Fig. 5a) confirms the efficiency of our applied acid-leaching procedures, as whole rock initial $^{87}Sr/^{86}Sr$ ratios are similar to primary magmatic values in most samples. Exceptions include a single volcanic whole rock sample (DR6-2) and the majority of plutonic rocks that are offset to radiogenic initial $^{87}Sr/^{86}Sr$ values at broadly similar initial $^{143}Nd/^{144}Nd$ ratios, which is consistent with the addition of seawater-derived Sr. The U-Th-Pb systems can also be disturbed by secondary processes, since U and Pb are mobile during low temperature and/or hydrothermal overprinting. In contrast, Th is generally considered to be resistant to alteration (e.g., Jochum and Verma, 1996; Verma, 1992). Average Nd/Pb and Nb/U values from the Investigator Ridge N- and E-MORB glasses are 15.8 ± 1.3 and 46.0 ± 2.3, respectively, whereas the Outsider Seamount glasses display Nd/Pb values of 6.3 ± 0.2 and Nb/U values of 32.4 ± 0.2 (Table S5). The Investigator Ridge whole rock samples processed for isotope analysis have an average Nd/Pb value of 15.9 ± 7.8 that is similar to the associated glasses, but the larger variability indicates some degree of Pb mobilization. Nb/U values from the whole rock samples are significantly shifted to lower values of 26.8 ± 16.8 (Investigator Ridge) and 23.7 (Outsider Seamount) compared to the respective glass rims. This effect is attributed to variable U addition to the rock samples from seawater during seafloor weathering. Over geological time scales, elevated U/Pb can result in higher amounts of ingrown ^{206}Pb by ^{238}U decay, while the ingrowth of ^{207}Pb is negligible in the age range of these rocks because of the high present-day $^{238}U/^{235}U$ value of 137.88. Reasonably good correlations in initial uranogenic (R^2 = 0.77) and thorogenic (R^2 = 0.86) Pb isotope spaces for the whole rocks and their overlap with associated glass (Fig. 6a, b) confirm that despite some secondary U addition and minor Pb mobilization, the initial isotope data reflect magmatic values and that U and Pb element mobility probably occurred shortly after the rock formed.

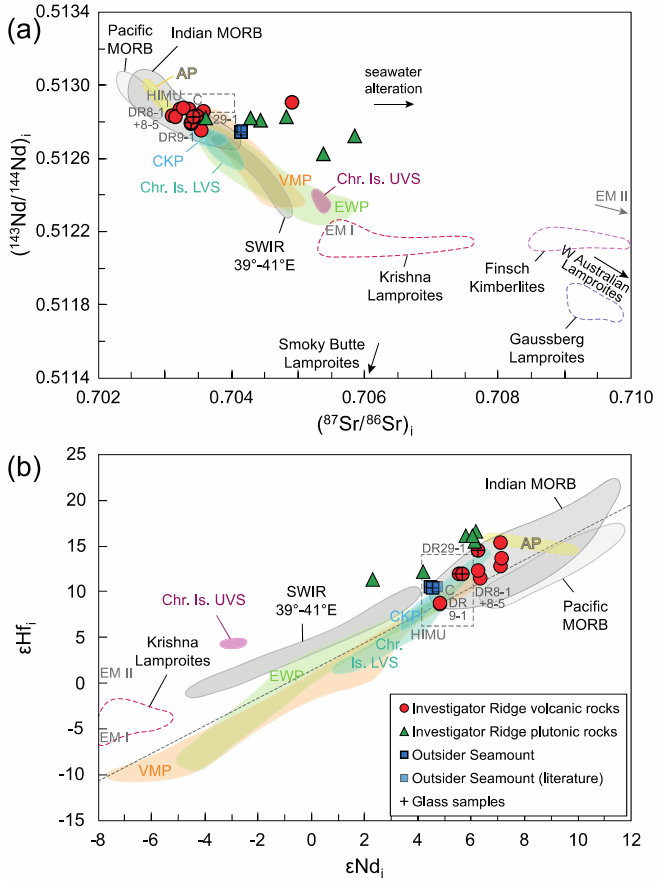

Fig. 5. Isotope correlation diagrams. (a) Initial $^{87}Sr/^{86}Sr$ versus $^{143}Nd/^{144}Nd$ diagram. The volcanic whole rock and glass samples cluster within the Indian MORB field and lie within the depleted end of the CHRISP field. Some of the plutonic samples have lower initial Nd ratios than the volcanic samples but most of them are shifted to higher $(^{87}Sr/^{86}Sr)_i$ ratios, probably largely due to post-magmatic seawater alteration effects. The Outsider Seamount samples display more enriched compositions than the Investigator Ridge volcanic rocks plotting at the enriched end of the Indian MORB field. (b) εNd_i versus εHf_i diagram showing that most of the volcanic rocks from the Investigator Ridge approximately lie on the Hf-Nd mantle array (dashed line), within the enriched part of the Indian MORB field and the depleted part of the CHRISP field. The plutonic samples, however, are shifted to more unradiogenic εNd_i values and therefore lie subparallel to the volcanic samples and outside the Indian MORB field. The Outsider Seamount samples plot at the most unradiogenic end of the Indian MORB field. Whole rock data from the Outsider Seamount are from Hoernle et al. (2011a), data for the CHRISP from Falloon et al. (2022), Hoernle et al. (2011a) and Taneja et al., 2016), for different lamproites and kimberlites from Chakrabarti et al. (2007), Murphy et al. (2002), Korsch and Gulson (1986), Nelson et al. (1986) and Fraser et al. (1985) and for Indian and Pacific MORB from PetDB at http://www.earthchem.org/petdb. Analytical errors are smaller than the symbol size.

Since the $^{40}Ar/^{39}Ar$ ages from our Investigator Ridge samples and from the literature data cover a large age range, we first calculated the initial isotopic compositions for our data using the measured parent/daughter ratios and the respective ages. We then projected all the literature and Investigator Ridge data to a common age of 100 Ma using estimated source parent/daughter ratios (Stracke et al., 2003; Willbold and Stracke, 2006; Workman and Hart, 2005) in order to compare the isotope data at a common source age. Measured and initial isotope data from this study are reported in Table S7. On initial $^{206}Pb/^{204}Pb$ versus $^{208}Pb/^{204}Pb$ and $^{207}Pb/^{204}Pb$ diagrams, the volcanic whole rock and glass samples from the Investigator Ridge form a fairly continuous positive array subparallel to the Northern Hemisphere Reference Line (NHRL) and are generally more enriched than Pacific MORB but lie within the Indian MORB field, excluding samples from the Southwest Indian Ridge (SWIR) between 39° and 41°E (Fig. 6a and b). The array extends from sample DR2-4 with $(^{206}Pb/^{204}Pb)_i$ = 17.88 at the depleted end to sample DR9-1 with $(^{206}Pb/^{204}Pb)_i$ = 18.72 at the enriched end. The samples with the most unradiogenic and the most radiogenic Pb isotopes correspond to the most incompatible-element depleted and enriched samples, respectively. Similarly, the volcanic rocks display a horizontal array overlapping with the Indian MORB field on the $(^{206}Pb/^{204}Pb)_i$ versus $(^{87}Sr/^{86}Sr)_i$ diagram (Fig. 3a of Supplementary Data 1) and a slight negative array on $(^{206}Pb/^{204}Pb)_i$ versus $(^{143}Nd/^{144}Nd)_i$ and $(^{176}Hf/^{177}Hf)_i$ diagrams (Fig. 6c and Fig. 3b of Supplementary Data 1). The samples also overlap with some of the CHRISP samples on the different isotope diagrams. However, on the $(^{206}Pb/^{204}Pb)_i$ versus $(^{207}Pb/^{204}Pb)_i$ and the $(^{206}Pb/^{204}Pb)_i$ versus $(^{176}Hf/^{177}Hf)_i$ diagrams, only the most enriched sample (DR9-1) overlaps with the Cocos-Keeling Volcanic Province (CKP) field, the westernmost province of the CHRISP.

Except for sample DR29-1, the Investigator Ridge plutonic samples generally have less radiogenic $(^{206}Pb/^{204}Pb)_i$ than the associated volcanic samples. With decreasing $(^{206}Pb/^{204}Pb)_i$ values, however, they do not continue the array formed by the volcanic samples that follows the Indian MORB field. Instead, the plutonic samples extend toward more radiogenic $(^{208}Pb/^{204}Pb)_i$ and $(^{207}Pb/^{204}Pb)_i$ and less radiogenic $(^{143}Nd/^{144}Nd)_i$ than Indian MORB. Specifically, they trend toward or overlap with the Eastern Wharton Basin Province (EWP) and to a lesser extent with the Vening-Meinesz Province (VMP) of the CHRISP (Fig. 6). Interestingly, in

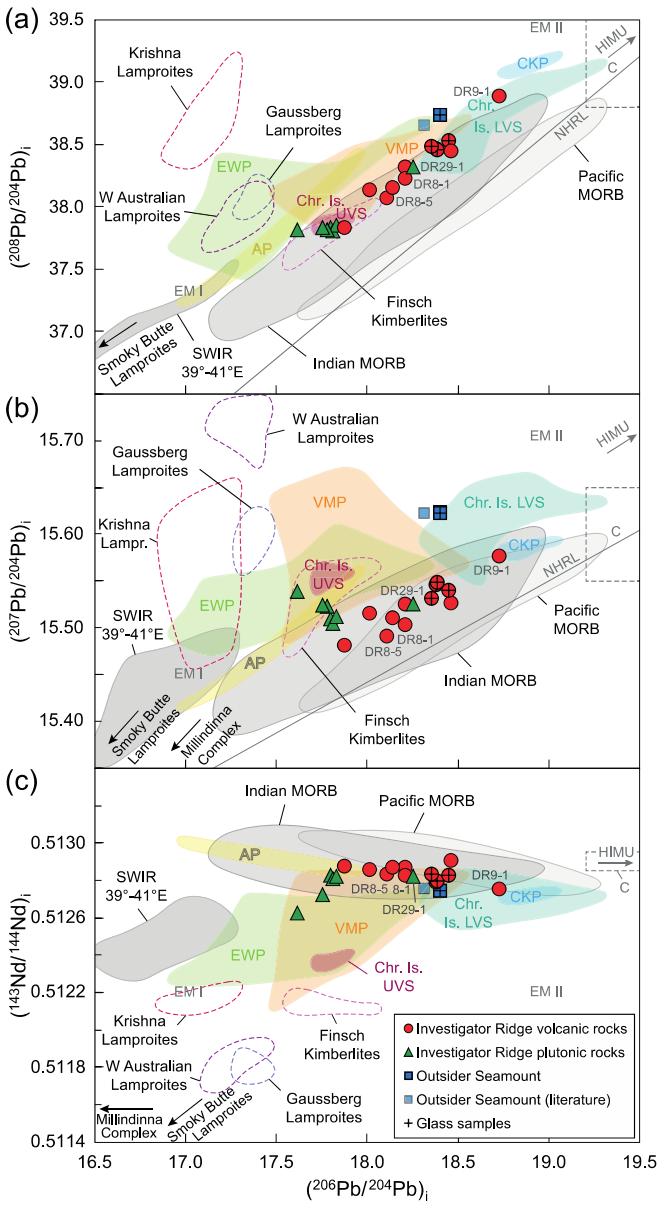

Fig. 6. Initial $^{206}Pb/^{204}Pb$ versus (a) $^{208}Pb/^{204}Pb$, (b) $^{207}Pb/^{204}Pb$ and (c) $^{143}Nd/^{144}Nd$ diagrams normalized to an age of 100 Ma (see text for details). In (a) and (b), the volcanic whole rock and glass samples from the Investigator Ridge form continuous positive arrays subparallel to the NHRL and plot within the Indian MORB field. Similarly, the volcanic rocks form a slight negative array within the Indian MORB field in (c). With one exception (DR29-1), the plutonic rocks plot at the depleted end of these arrays and trend towards more unradiogenic $(^{206}Pb/^{204}Pb)_i$ and $(^{143}Nd/^{144}Nd)_i$, but at the same time towards more radiogenic $(^{208}Pb/^{204}Pb)_i$ and $(^{207}Pb/^{204}Pb)_i$ values in the direction of Gaussberg (Antarctica), Krishna (India) and West Australian lamproites and overlap with Finsch kimberlites (S Africa). On a more local scale, the Investigator Ridge intrusive rocks overlap with the upper volcanic series (UVS) of Christmas Island in thorogenic Pb isotope space (a) and trend toward the UVS in uranogenic Pb space (b). The samples from the Outsider Seamount are similar to the Investigator Ridge volcanic samples in terms of initial Nd isotope ratios but display distinctly higher $(^{208}Pb/^{204}Pb)_i$ and $(^{207}Pb/^{204}Pb)_i$ values similar to the CHRISP samples. Data sources are the same as in Fig. 5. Analytical errors are smaller than the symbol size.

Pb-Pb isotope space the plutonic samples overlap with (Fig. 6a) and trend towards (Fig. 6b) the upper volcanic series (UVS) of Christmas Island. In Nd-Hf isotope space, the plutonic rocks are roughly correlated and stretch subparallel to but above the Indian MORB/SWIR 39-41°E arrays, with a faint trend toward the UVS field (Fig. 5b). Sample DR29-1 differs from the other plutonic samples and shows a higher $(^{206}Pb/^{204}Pb)_i$ value overlapping with the moderately enriched volcanic rocks in all isotope diagrams.

The whole rock and glass samples from the Outsider Seamount have initial $^{206}Pb/^{204}Pb$, $^{143}Nd/^{144}Nd$ and $^{176}Hf/^{177}Hf$ values similar to the moderately enriched Investigator Ridge samples but they display distinctly higher initial $^{208}Pb/^{204}Pb$, $^{207}Pb/^{204}Pb$ and $^{87}Sr/^{86}Sr$ values that overlap with the CHRISP.

4. Discussion

4.1. Correlation of $^{40}Ar/^{39}Ar$ ages with magnetic chron ages along the Investigator Ridge

Our new $^{40}Ar/^{39}Ar$ ages cover much of the geographical extent of the Investigator Ridge from ~ 9-17°S and thus allow us to examine magmatic geochemistry with age. The geochronology shows a clear spatial age progression from 100.0 to 83.0 Ma for stations DR23, DR10 and DR6 with the samples becoming younger with decreasing southern latitudes (R^2 = 0.91; Fig. 7a). Samples DR8-5 and DR29-1 clearly deviate from this age progressive trend, as they are ~ 23 and 45 Ma younger than expected, respectively. Therefore, they may belong to a later magmatic event, presumably the CHRISP volcanism, which will be discussed in more detail in Section 4.3. The observed age progression is consistent with the regional E-W strike of the magnetic lineation in this region and the northward decrease of magnetic chron ages (Sclater and Fisher, 1974, Liu et al., 1983; Jacob et al., 2014). Therefore, it is likely that the recovered rocks formed during seafloor spreading at the now extinct and subducted WSC located north of the Investigator Ridge, and that the Investigator Ridge belongs to a fracture zone (FZ) related to a ridge transform fault of the WSC (Jacob et al., 2014; Liu et al., 1983). This is further supported by the average half-spreading rate of 36.4 mm/a calculated from our 100.0 to 83.0 Ma $^{40}Ar/^{39}Ar$ ages, which mostly cover the Cretaceous Normal Superchron (CNS; chron C34, ~121–84 Ma) – a time period in which deduction of spreading rates by magnetic seafloor anomalies is not possible. Our calculated half-spreading rate is only slightly slower than that of 38.6–42.3 mm/a obtained for the ~ 84–68 Ma interval inferred from chrons 34–31 on both sides of the FZ (Fig. 7; Jacob et al., 2014). Consequently, our $^{40}Ar/^{39}Ar$ dating results should approximately match the corresponding chron ages and potentially extend ground-truthed crustal ages well into the CNS.

However, some difficulties arise when comparing the $^{40}Ar/^{39}Ar$ ages with the chron ages due to the tectonic complexity of the area. First of all, the chrons west and east of the Investigator FZ are left-laterally offset by ~ 800–900 km (~6–7 chrons) meaning that the crust west of the FZ is around 15–20 Ma younger than the crust in the east. It is therefore crucial to know from which side of the FZ the dredged rocks originate in order to relate their $^{40}Ar/^{39}Ar$ ages to the correct crustal ages and to extrapolate ages for undated rocks and sampling sites. Furthermore, the inferred age progression based on geochronology only applies if samples belong to the same side of the FZ. During SO199, the rocks were generally recovered along the steep west-facing slope of the Investigator Ridge implying derivation from the crust on the western side of the FZ, assuming that the FZ runs along the center of the ridge. However, the ridge-like morphology of the Investigator FZ is counterintuitive, since FZs form at the terminations of ridge transform faults which are usually deep troughs that are merged to zero age oceanic crust at the ridge-transform intersection (RTI) to become a FZ (Grevemeyer et al., 2021 and references therein). Therefore, FZs usually form troughs, although filling of the transform fault trough by volcanism at the RTI can also occur

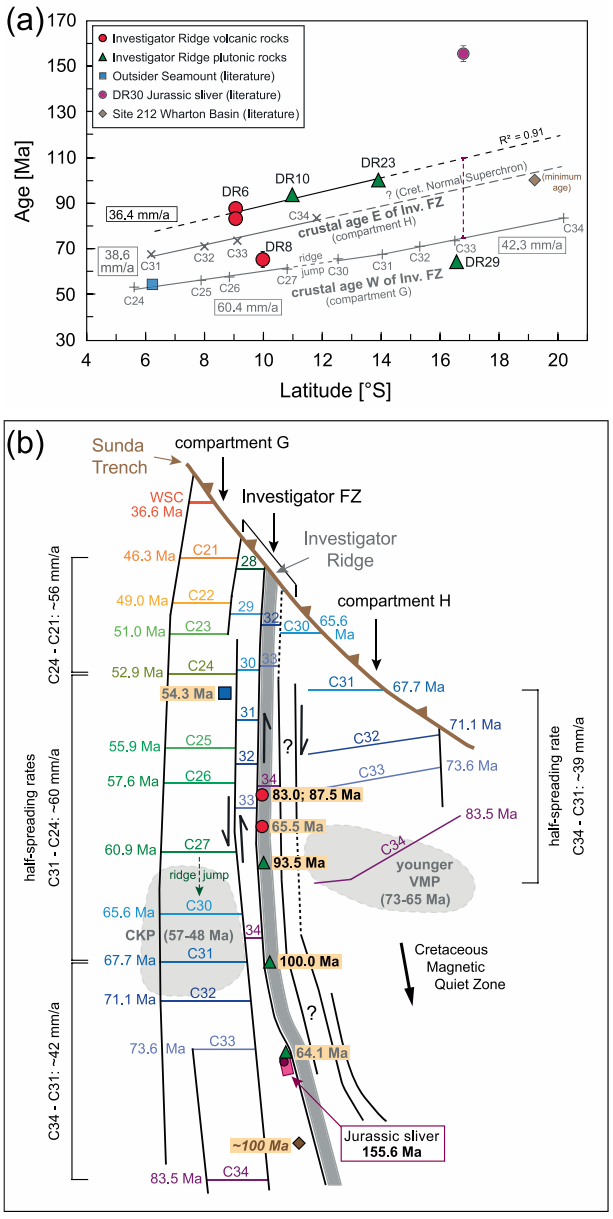

Fig. 7. (a) Latitude °S versus $^{40}Ar/^{39}Ar$ age showing the age progression along the Investigator Ridge resulting in an average half-spreading rate of 36.4 mm/a (black solid and dashed line). Exceptions are samples DR8-5 (located in the central part of the ridge) and DR29-1 (located in the south at the ridge-like structure west of the ridge) with distinctly younger ages deviating from the trend. These two samples are interpreted to have formed by later CHRISP volcanism, thus they were excluded from the determination of the DR6 to DR23 regression line. Chron age trends for the oceanic crust from west (compartment G) and east (compartment H) of the Investigator FZ system (gray solid lines) are derived from the magnetic lineations identified by Jacob et al. (2014; see Fig. 1b), using the time scale of Seton et al. (2012). Since the chron ages south of C34 are unknown due to the Cretaceous Normal Superchron, crustal ages can only be estimated by extrapolation of spreading rates. The average half-spreading rates of 42.3 mm/a in compartment G and 38.6 mm/a in compartment H between chrons C34 and C31 (83.5–67.7 Ma) are fairly similar to the 36.4 mm/a trend derived from our $^{40}Ar/^{39}Ar$ ages. Recalculated $^{40}Ar/^{39}Ar$ ages from the Outsider Seamount and the DR30 Jurassic sliver are from Hoernle et al. (2011a) and Gibbons et al. (2012), respectively. The minimum age of the basaltic basement at Site 212 is assumed to be 100 Ma (von der Borch et al., 1974; see text for details). The 2σ/95 % confidence $^{40}Ar/^{39}Ar$ age errors are typically smaller than the symbol size, otherwise error bars are shown. (b) Sketch illustrating the assumed offsets of crustal ages within the Investigator FZ system based on the new $^{40}Ar/^{39}Ar$ ages from this study combined with the location and corresponding chron ages from Jacob et al. (2014); see text for details. Half arrows indicate the direction of the spreading axis offset. The assumed distances of the magnetic lineations younger than C30 are derived from compartment F, located west of compartment G (Jacob et al., 2014), as C29 and C28 are missing in compartment G due to a local ridge jump.

(Grevemeyer et al. 2021). It is not yet possible to solve the complexities of FZ formation for the distant geological past in the absence of an active ridge transform fault as is the case here. For now, we assume that the Investigator Ridge formed on one side of the FZ rather than the FZ running through the center of the ridge. In the northern part, however, the Investigator Ridge is subdivided into two parallel ridges with a basin in-between (Fig. 2a) that could possibly mark the trace of the FZ. Ridge-like structures, the so-called (oceanic) transverse ridges (Bonatti, 1978), have been observed along large offset FZs in the equatorial Atlantic Ocean such as the Romanche, Vema, Kane and Chain FZs (e.g., Bonatti, 1978; Gasperini et al., 2017; Marjanović et al., 2020; Pockalny et al., 1996). In the Indian Ocean, transverse ridges have so far only been reported for the Owen FZ (Carlsberg Ridge) and the Atlantis II FZ (SWIR; Bonatti, 1978; Dick et al., 1991; Muller et al., 2000). Transverse ridges are defined as topographic highs that run parallel to a FZ within a distance of 50 km, are usually less than 50 km wide and have an asymmetric morphology with a steep FZ-facing wall and a gentle slope on the opposite side. They can reach lengths of 50 to 1000 km and mostly run along the older lithospheric block but can also be present on both sides of a FZ (e.g., Bonatti, 1978; Pockalny et al., 1996). The origin of such ridges is still controversial but it is assumed that they form by tectonic uplift of upper mantle and crustal blocks, presumably in conjunction with a global plate reorientation and thus changes in spreading direction (e.g., Marjanović et al., 2020; Pockalny et al., 1996). The Investigator Ridge generally shares the characteristics of a transverse ridge, and the recovery of a large variety of rock types from the upper and lower crust and upper mantle exposed at the steep west-facing slope of the ridge requires tectonic uplift. In conclusion, the rocks sampled on the Investigator Ridge are considered to broadly belong to the same vertical strip of oceanic crust and can thus be correlated with each other.

SO199 bathymetric mapping provides some information about the position of the FZ relative to the Investigator Ridge. The asymmetric dip of its western and eastern slopes is typical for a transverse ridge and implies that the Investigator FZ is located west of the ridge. Additionally, the steep western slope shows signs of recent tectonic activity, such as sparse sediment cover, relatively thin oxidation/weathering rinds of the recovered rocks and the absence of sessile invertebrates, indicating frequent movements at the slope (Werner et al., 2009). Young deformation is supported by faulted surface sediments, N-S oriented ravines and asymmetric tops of seamounts adjacent to the ridge such as the Outsider Seamount (Fig. 2d; Werner et al., 2009). Furthermore, seismic activity with left-lateral strike-slip motion in the Wharton Basin is recorded by recent intraplate earthquakes with magnitudes of up to 8.6. One of them is located directly west of the central Investigator Ridge, implying reactivation of older seafloor fabrics related to the development of a diffuse new plate boundary between the western and eastern parts of the Indo-Australian plate (e.g., Deplus, 2001; Deplus et al., 1998; Duputel et al., 2012; Gordon et al., 1990; Lay et al., 2016). Since the current deformation occurs along pre-existing tectonic structures, the Investigator FZ likely runs along the steep west-facing slope of the ridge and thus the recovered magmatic rocks originate from the eastern part of the oceanic crust. Interestingly, the current deformation pattern is left-lateral along N-S striking FZs that originate from right-lateral transform faulting of the WSC, implying reversal of the shear sense. We speculate that tectonic reactivation in this case requires excessive force to overcome the paleo-fabrics and may contribute to the recorded high-energy earthquakes (e.g., Duputel et al., 2012; Lay et al., 2016).

When comparing our $^{40}Ar/^{39}Ar$ ages from the magmatic rocks (excluding the two distinctly younger CHRISP-related samples DR8-5 and DR29-1) with the chron ages on both sides of the Inves-

tigator Ridge, it becomes clear that they do not fit the chron ages of either side. Our $^{40}Ar/^{39}Ar$ ages are systematically ~ 30 Ma older than the corresponding chron ages on the western side (Fig. 1b and 7a), clearly excluding their direct assignment to the available magnetic lineations on this side. The problem, however, is that our $^{40}Ar/^{39}Ar$ ages from the Investigator Ridge are also ~ 11 Ma older than the chron ages on the eastern side (Fig. 7b). A more detailed consideration of the tectonic situation yet shows that the identified magnetic lineations on both sides do not reach the ridge. On the western side, they terminate ~ 30–50 km west of the ridge, apparently along a second FZ running parallel to the Investigator Ridge. Parts of this second FZ were observed as a N-S striking bathymetric depression during cruise SO199 (Werner et al., 2009). Interestingly, Liu et al. (1983) mark the course of the Investigator FZ as a combination of the course of the Investigator Ridge (in the north) and the second FZ (in the south) in their Fig. 2, treating the two FZs as a single FZ. At first glance, it thus seems that the magnetic lineations to the west defined by Liu et al. (1983) reach the Investigator Ridge, which illustrates that the structure of the Investigator FZ could not be fully explored in detail at that time. More recently, Jacob et al. (2014) presented an updated tectonic map of fracture zones and magnetic lineations in the Wharton Basin and describe the Investigator FZ as having multiple FZs; the only such in the Wharton Basin besides a number of single and double FZs. Their findings highlight the complexity of this tectonic system containing at least three subparallel N-S striking FZs, with the Investigator Ridge itself being only one part of this system. Unfortunately, no magnetic lineations within the narrow strips of oceanic crust between the individual FZs of the Investigator FZ system have been identified so far and therefore, the chrons immediately west of the Investigator Ridge are currently unknown. The same applies to the oceanic crust directly east of the ridge, since the available magnetic lineations seem to end at another FZ in the east (Fig. 1b; Jacob et al., 2014). An additional uncertainty on this side arises from the fact that south of ~ 12°S, the crust formed during the CNS. Therefore, crustal ages can only be extrapolated assuming roughly stable spreading rates. Furthermore, at least one fossil spreading ridge (at about 11°S) is presumably embedded in the crust east of the Investigator Ridge suggesting one or more local ridge jumps, thus making the tectonic reconstruction even more complicated.

The unknown ages of the narrow oceanic crust segments directly west and east of the Investigator Ridge prevent a precise determination of the lateral displacements along the different fault zones of the Investigator FZ system. In addition, the displacements cannot be inferred from the segmentation of the fossil WSC either, since this part is already subducted at the Sunda Trench. However, our new $^{40}Ar/^{39}Ar$ ages from the ridge allow the addition of some constraints. As part of the oceanic crust directly east of the ridge, the $^{40}Ar/^{39}Ar$ ages reflect the age of this crust segment between two Investigator FZs. Relative to the crust with identified chrons in the west, referred to as compartment G by Jacob et al. (2014; Fig. 7b), there must be a left-lateral offset of the WSC axis of ca. 1,200–1,300 km to account for the age difference of ~ 30 Ma across the FZ. It is, however, likely that the narrow strip between compartment G and the Investigator Ridge is also offset, and Leg 22 Site 212 drilled at the southern end of the ridge may give an indication of the extent of this offset. According to the locations of the FZs from Jacob et al. (2014), Site 212 was drilled east of the FZ running along the Investigator Ridge (Fig. 1b). However, since the ridge bends toward a more NNW-SSE direction in its southern part, we propose that the trace of the FZ is imprecisely defined and is shifted more towards the east, therefore Site 212 is actually located on oceanic crust between the ridge and compartment G (Fig. 7b). Although the drilled basaltic basement at Site 212 has not been dated, a minimum age of 100 Ma is assumed based on the extrapolated age of the overlying sediment, which gives an age range of 85–110 Ma (inferred from assumed sedimentation rates) with a mean age close to 100 Ma at the contact with the basement (von der Borch et al., 1974). Site 212 is aligned with crust that is ~ 18 Ma younger to the west (compartment G) and it should be aligned with crust that is ~ 16 Ma older to the east (Investigator Ridge), since it is situated ~ 600 km to the south of the location of DR23 with a similar age (100.0 ± 2.0 Ma; 95 % conf.; Fig. 7b). Therefore, nearly half of the total left-lateral ridge offset seems to have taken place along the FZ that runs directly west of the Investigator Ridge. In contrast, on the opposite side, east of the Investigator Ridge, we suggest a right-lateral offset of the paleo WSC axis relative to the crust segment with known chrons further east, referred to as compartment H by Jacob et al. (2014; Fig. 7b). Although solely left-lateral displacements of chron ages have been observed at FZs in the Eastern Indian Ocean east of the Ninetyeast Ridge so far, a right-lateral offset of about 450 km would explain our Investigator Ridge $^{40}Ar/^{39}Ar$ ages being ~ 11 Ma older than the corresponding oceanic crust of compartment H. We cannot, however, constrain whether an additional crust segment exists between this ridge strip and compartment H as indicated by Jacob et al. (2014) and if so, how it is displaced relative to these segments.

The two literature $^{40}Ar/^{39}Ar$ ages from the Investigator Ridge using SO199 samples relate to the WSC history as follows. Sample DR1-10 from the Outsider Seamount (Hoernle et al. 2011a), located ~ 80 km west of the Investigator Ridge, has a recalculated age of 54.32 ± 0.32 Ma and the seamount is situated near chron C24r oceanic crust (53.3 Ma; Seton et al., 2012). The 54.3 Ma age also lies on the regression line of the chron ages located west of the Investigator Ridge (compartment G) between chrons 31 and 24 (Fig. 7a). Therefore, the Outsider Seamount apparently formed as a near-ridge seamount at or near the WSC. Glass sample DR30 was recovered from one of the plateau-like structures directly west of the southern part of the Investigator Ridge and is located immediately west of the FZ running along the western base of the Investigator Ridge. However, the Late Jurassic recalculated $^{40}Ar/^{39}Ar$ age of 155.6 ± 3.4 Ma (Gibbons et al., 2012) is distinctly older than expected crustal ages in this area. Based on our considerations discussed above, the crustal age at this location should either range from ~ 75 Ma (the chron age west of the strip) to ~ 110 Ma (extrapolated from our $^{40}Ar/^{39}Ar$ ages from the Investigator Ridge; see dark red vertical dashed line in Fig. 7a), or it should be ~ 93 Ma (extrapolated from the ~ 100 Ma basement age of Site 212 and using a half-spreading rate of ~ 40 mm/a). Thus, the 155.6 Ma DR30 $^{40}Ar/^{39}Ar$ age does not fit any of the age progressive trends in the region. This supports the conclusion of Gibbons et al. (2012), based on their tectonic reconstructions, that glass sample DR30 cannot have formed in the framework of the creation of the Investigator FZ and the surrounding oceanic crust. Instead, they suggest that it belongs to a tectonic sliver (the plateau-like structure) formed at the Argo spreading ridge, which initially separated Argoland north of East Gondwana from Australia and Greater India ~ 155 Ma ago and was transferred to its present-day location after several spreading reorganizations and ridge jumps.

4.2. Geochemical characteristics of the Investigator Ridge

As shown in Figs. 3 to 6, igneous rocks from the Investigator Ridge display a large compositional range in terms of trace elements and radiogenic isotope ratios. Considering their formation at a mid-ocean spreading center, tholeiitic MORB type compositions reflecting large degrees of melting are expected. The substantial geochemical variability ranging from element-depleted N-MORB to more enriched E-MORB tholeiites and sparse transitional alkaline to alkaline basalts, however, implies variably enriched source materials and extents of melting. The low

TiO_2/Yb ratios within the MORB array and flat HREE patterns of most samples indicate shallow melting consistent with formation at a spreading center, except for the three most enriched samples (DR8-1, DR8-5 and DR9-1) pointing to a slightly deeper and shorter melt interval (Figs. 3 and 4). In the following, we will further investigate the processes that led to these geochemical characteristics.

Initial radiogenic isotope compositions of the Investigator Ridge igneous rocks provide information about the paleo-composition and evolution of the Indian oceanic mantle in this region. On various isotope correlation diagrams, the samples lie within the Indian MORB field at 100 Ma (Figs. 5, 6 and Fig. 3 of Supplementary Data 1) and mirror the DUPAL-like compositions of typical Indian (and South Atlantic) MORB magmas. In general, they are isotopically more enriched than North Atlantic and Pacific MORBs with higher $^{207}Pb/^{204}Pb$, $^{208}Pb/^{204}Pb$, $^{87}Sr/^{86}Sr$ and lower $^{143}Nd/^{144}Nd$ at a given $^{206}Pb/^{204}Pb$. Similar to the Indian MORB field, the samples form an array between components with high and low $^{206}Pb/^{204}Pb$ ratios. The component with radiogenic $^{206}Pb/^{204}Pb$ ratios may be represented by a moderately HIMU-like component, such as the common "C" or "FOZO" (Focal Zone) type components. The "C" component, defined by Hanan and Graham (1996), and FOZO, originally defined by Hart et al. (1992) and Hauri et al. (1994) and redefined by Stracke et al. (2005), are very similar and are assumed to represent a large part of the lower mantle containing young (~300–2000 Ma) recycled oceanic crust, which is sampled by both MORBs and OIBs. At low $^{206}Pb/^{204}Pb$ ratios, the volcanic samples from the Investigator Ridge and Indian (and South Atlantic) MORBs in general require both an enriched (enriched mantle one (EMI) type) and a depleted (DM) endmember unlike North Atlantic and Pacific MORBs that only require a DM type component. Therefore, the volcanic samples recovered at the Investigator Ridge represent typical Indian upper mantle compositions, and our data show that the Indian upper mantle has preserved this specific isotopic composition since at least ~ 100 Ma ago.

The Investigator Ridge plutonic rocks, in contrast, have isotopic compositions different from those of the volcanic rocks, even when compared with volcanic rocks from the same dredge site. The plutonic samples trend toward an enriched component that is characterized by more radiogenic $^{208}Pb/^{204}Pb$, $^{207}Pb/^{204}Pb$ and less radiogenic Nd isotope ratios (Fig. 6 and Fig. 3 of Supplementary Data 1). Therefore, a further enriched component in addition to those involved in the volcanic rocks is required. But what kind of source is responsible for this enriched isotopic flavor and why is it only observed in the plutonic rocks?

A closer inspection of isotopic compositions in the nearby CHRISP may help to constrain this additional enriched source component. The CHRISP compositions overlap with those of the Investigator Ridge in most of the radiogenic isotope correlation diagrams, spanning a large range between low and high $^{206}Pb/^{204}$-Pb. Vitally, however, the CHRISP samples also extend to more radiogenic initial $^{208}Pb/^{204}Pb$, $^{207}Pb/^{204}Pb$ and $^{87}Sr/^{86}Sr$ and less radiogenic $^{143}Nd/^{144}Nd$ and $^{176}Hf/^{177}Hf$ similar to the plutonic rocks from the Investigator Ridge and trend towards or overlap with various lamproites and kimberlites from Australia, Antarctica, India and South Africa (Figs. 5, 6 and Fig. 3 of Supplementary Data 1). Hoernle et al. (2011a) proposed that the CHRISP formed through decompression melting of delaminated subcontinental lithospheric mantle (SCLM) that contains components similar to lamproites from Australia and India which derive from metasomatized continental lithospheric mantle and is mixed with MORB material at or near a mid-ocean ridge. Since the CHRISP formed shortly after breakup of East Gondwana, it is feasible that continental material delaminated during breakup and was entrained in the upper mantle. Therefore, such shallow recycling of SCLM material could also account for the compositions of the Investigator Ridge samples. In particular, the low proportions of the SCLM signal recorded in the plutonic samples are intriguing as they formed at or near the spreading center where the upper mantle MORB signal dominates. It can only be hypothesized why this signature is more prominent in the plutonic samples. It is conceivable that off-axis low degrees of melts preferentially tapped the enriched and likely more fusible SCLM source material and that such melts could have intruded young, off-axis crust and thereby preserved the SCLM flavor, whereas this flavor was diluted by the longer melt column beneath the ridge axis and thus is not recorded in the WSC volcanics.

4.3. Investigator Ridge igneous record: Its relation to CHRISP and the Indian MORB source

Since the Investigator FZ and the CHRISP are closely located to each other and their igneous rocks display similar geochemical characteristics, we will now evaluate the formation of these structures in a common tectonic framework, using available $^{40}Ar/^{39}Ar$ ages and tectonic reconstructions. Hoernle et al. (2011a) divided the CHRISP into four different volcanic sub-provinces with decreasing ages from east to west: the Argo Basin Province (AP) with a recalculated $^{40}Ar/^{39}Ar$ age of 138.4 Ma, the Eastern Wharton Basin Province (EWP) being 117.8–95.8 Ma old, the Vening-Meinesz Province (VMP) 97.2–64.5 Ma old and the Cocos-Keeling Province (CKP) 57.0–47.5 Ma old (Fig. 1a). Christmas Island located in the north of the eastern VMP is considerably younger than the VMP. The island comprises two volcanic phases, the Eocene Lower Volcanic Series (LVS; 44.3–37.6 Ma) and the Pliocene rejuvenated Upper Volcanic Series (UVS; recalculated to 5.1–3.1 Ma; Falloon et al., 2022; Hoernle et al., 2011a). The western portion of the CHRISP crosses the Investigator Ridge and VMP and CKP volcanism took place near the already existing Investigator Ridge (Figs. 1 and 7b). As discussed in Section 4.1, our new $^{40}Ar/^{39}Ar$ ages show an age progression along the Investigator Ridge, except for samples DR8-5 and DR29-1 that are ~ 23–29 Ma younger than expected according to their location on oceanic crust generated by mid-ocean ridge spreading (Fig. 7a and b). Instead, our $^{40}Ar/^{39}Ar$ ages of 65.5 and 64.1 Ma are similar to the youngest VMP seamounts in the vicinity of the ridge (VMP age range is recalculated to 72.8–64.5 Ma) and are only slightly older than the recalculated 57.0–47.5 Ma range of CKP seamounts (Hoernle et al., 2011a). Therefore, it is likely that samples DR8-5 and DR29-1 are part of the CHRISP volcanism rather than of the Investigator Ridge and formed after construction of the Investigator FZ and associated ridge. This indicates that the CHRISP volcanism also occurred across this tectonic structure and between the VMP and CKP sub-provinces. The affiliation of the two young Investigator Ridge samples to the CHRISP volcanism is further supported by their geochemistry. The CHRISP samples generally display more enriched compositions than those from the Investigator Ridge, except for these two samples plus samples DR8-1 (from the same dredge as dated sample DR8-5) and DR9-1 (recovered slightly further south), which fall within the CHRISP field on multielement diagrams and on various diagrams of incompatible element ratios and trend towards OIB compositions (Figs. 3 and 4). Although the two latter samples could not be dated, it is possible that they have similarly young ages as samples DR8-5 and DR29-1, and these four enriched samples can presumably be regarded as part of the CHRISP. Furthermore, the 54.3 Ma old Outsider Seamount has comparable geochemical compositions and likely also formed in the framework of the CHRISP volcanic event.

The various radiogenic isotope plots (Figs. 5, 6 and Fig. 3 of Supplementary Data 1) reveal that the sub-provinces of the CHRISP differ in their isotopic compositions. Whereas the AP, the oldest province in the east, shows more depleted compositions and largely overlaps with the Indian MORB field, the EWP west of the

AP has more enriched compositions and extends towards the enriched SCLM component and Krishna lamproites. The field for the more westerly and younger VMP partly overlaps with that of the EWP but extends to more radiogenic $(^{206}Pb/^{204}Pb)_i$ values and at the same time more in the direction of W Australian and Gaussberg lamproites that display very high $(^{207}Pb/^{204}Pb)_i$ ratios. In contrast, the youngest portions of the CHRISP, the CKP and the Christmas Island LVS, show fairly high $(^{206}Pb/^{204}Pb)_i$ ratios and overall higher Nd and Hf but lower Sr isotope ratios than the EWP and VMP and plot near common "C" or "FOZO" compositions in all diagrams (Figs. 5, 6 and Fig. 3 of Supplementary Data 1). This implies that the composition of the source region in the CHRISP area changed with time, which may also be the case for spreading center volcanism recorded at the Investigator Ridge. In fact, a combination of geochemical and age data reveals good linear correlations of the $^{40}Ar/^{39}Ar$ ages with incompatible trace element ratios, such as $(La/Sm)_N$ (R^2 = 0.79 or 0.92 when excluding subvolcanic sample DR6-2; Fig. 8a), $(Sm/Yb)_N$ (Fig. 8b) and $(La/Yb)_N$ (R^2 = 0.42 and 0.78, respectively; and excluding DR6-2 improves the R^2 value to 0.92 and 0.94, respectively). The $^{40}Ar/^{39}Ar$ data also show good correlations with $(La/Nd)_N$, $(Nb/Ta)_N$ and Nb/Y (R^2 = 0. 82–0.83), $(La/Ce)_N$ (R^2 = 0.78), $(Nb/Zr)_N$ (R^2 = 0.63) and (Nb, Th, TiO_2)/Yb (R^2 = 0.47–0.84), showing higher ratios and thus more enriched compositions with decreasing ages. Such systematic variations with age can also be observed for initial $^{206}Pb/^{204}Pb$ ratios (R^2 = 0.57; excluding DR6-2: R^2 = 0.93; Fig. 8c) and $^{208}Pb/^{204}Pb$ (R^2 = 0.66; excluding DR6-2: R^2 = 0.81; Fig. 8d) and to a lesser extent for Hf isotopes (R^2 = 0. 61), but no systematic variations with age are observed for $^{207}Pb/^{204}Pb$, Nd and Sr isotope data (not shown). As demonstrated in Fig. 8, samples from the CHRISP sub-provinces yield comparable correlations, although they are only very weak in terms of $(La/Sm)_N$, and the CHRISP samples generally have more enriched trace element compositions. However, their $(^{206}Pb/^{204}Pb)_i$ and $(^{208}Pb/^{204}Pb)_i$ isotopic compositions overlap with those from the Investigator Ridge and they show a similar increase in ratios with decreasing ages and thus from the oldest province in the Argo Basin (AP) in the east, westwards to EWP and the VMP, and finally toward the youngest CKP and the Christmas Island LVS.

These observations have implications for the formation history of the Investigator Ridge and CHRISP and for the characterization of the Indian Mantle Domain in this region. Combining the geochemical characteristics with the tectonic reconstructions for the Eastern Indian Ocean, the evolution of the Investigator Ridge and the CHRISP can be linked, as they formed in proximity of the same spreading system, namely the WSC, and physically tapped the same mantle region. The oldest dated samples from the Investigator Ridge (100.0–93.5 Ma) formed contemporaneously with the EWP (117.8–95.8 Ma) and with the oldest part of the VMP (97.2–83.4 Ma), and they overlap in radiogenic isotope compositions with these two provinces (Fig. 9a and b). The 83.0 Ma old Investigator Ridge sample also formed during emplacement of the older VMP (Fig. 9b) and has similar $(^{208}Pb/^{204}Pb)_i$ ratios but is shifted towards higher $(^{206}Pb/^{204}Pb)_i$. The two youngest (65.5–64.1 Ma) samples found on/near the Investigator Ridge overlap with the younger part of the VMP (72.8–64.5 Ma) both in terms of ages and geochemical compositions, thus supporting the assumption that they can be regarded as part of the CHRISP volcanism (Fig. 9c). The fact that these two samples, although belonging to the CHRISP, form good correlations with the samples clearly belonging to the Investigator Ridge confirms that the ridge and the CHRISP share the same formation history. The differences in trace element compositions with the CHRISP rocks being more enriched may be attributed to the Investigator Ridge samples having formed directly at the ridge axis with high degrees of melting resulting from long melt columns. In contrast, the CHRISP volcanism occurred at some distance from the spreading ridge (although still in the vicinity), and is up to 25 Ma younger than the underlying oceanic crust (Hoernle et al.,

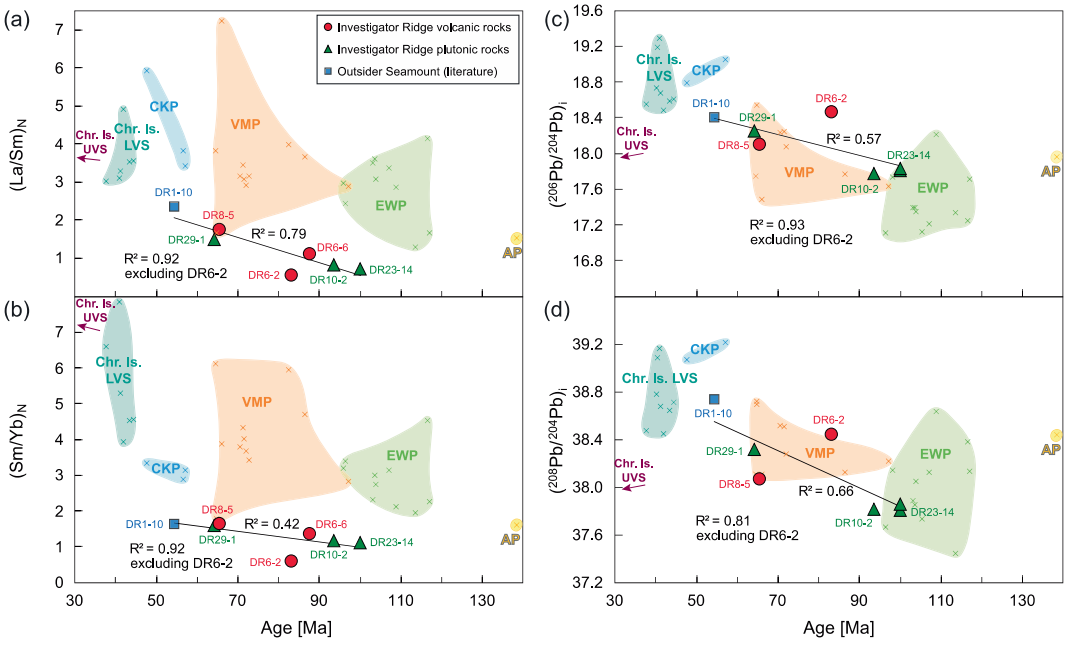

Fig. 8. $^{40}Ar/^{39}Ar$ age in million years versus (a) $(La/Sm)_N$, (b) $(Sm/Yb)_N$, (c) $(^{206}Pb/^{204}Pb)_i$ and (d) $(^{208}Pb/^{204}Pb)_i$ diagrams. The samples from the Investigator Ridge including the Outsider Seamount show moderate to good linear correlations (R^2 = 0.42–0.79) with increasing incompatible element and Pb isotope ratios and thus more enriched compositions from older to younger samples. Excluding subvolcanic sample DR6-2, which slightly deviates from the trend by showing more depleted trace element and more enriched isotope characteristics, the R^2 increases to 0.81–0.93. The CHRISP samples also display a slight increase in $(La/Sm)_N$ and $(Sm/Yb)_N$ ratios with decreasing ages (a + b) but generally have more enriched compositions than the Investigator Ridge samples. It must be noted, however, that the correlation coefficient for $(La/Sm)_N$ is very low (R^2 = 0.14), whereas it improves for $(Sm/Yb)_N$ with R^2 = 0.67 (including Christmas Island UVS). A pronounced linear correlation is observed for Pb isotope ratios of the CHRISP samples (c + d) with R^2 = 0.64 for $(^{206}Pb/^{204}Pb)_i$ and 0.44 for $(^{208}Pb/^{204}Pb)_i$, and the values overlap with those of the Investigator Ridge samples in the respective age ranges. Christmas Island UVS is excluded from correlations in isotope space as it represents rejuvenated petit-spot volcanism involving a purer signal of the recycled SCLM component. Data sources are the same as in the previous figures.

2011a), thus leading to lower overall degrees of melting as a consequence of shorter melt columns under a thicker lithosphere. The generally more depleted $^{208}Pb/^{204}Pb$ and $^{207}Pb/^{204}Pb$ and Nd and Hf isotope ratios of the Investigator Ridge samples compared to the CHRISP and their large overlap with the Indian MORB field could be explained by melting of higher proportions of depleted upper mantle material and dilution of the enriched component(s).

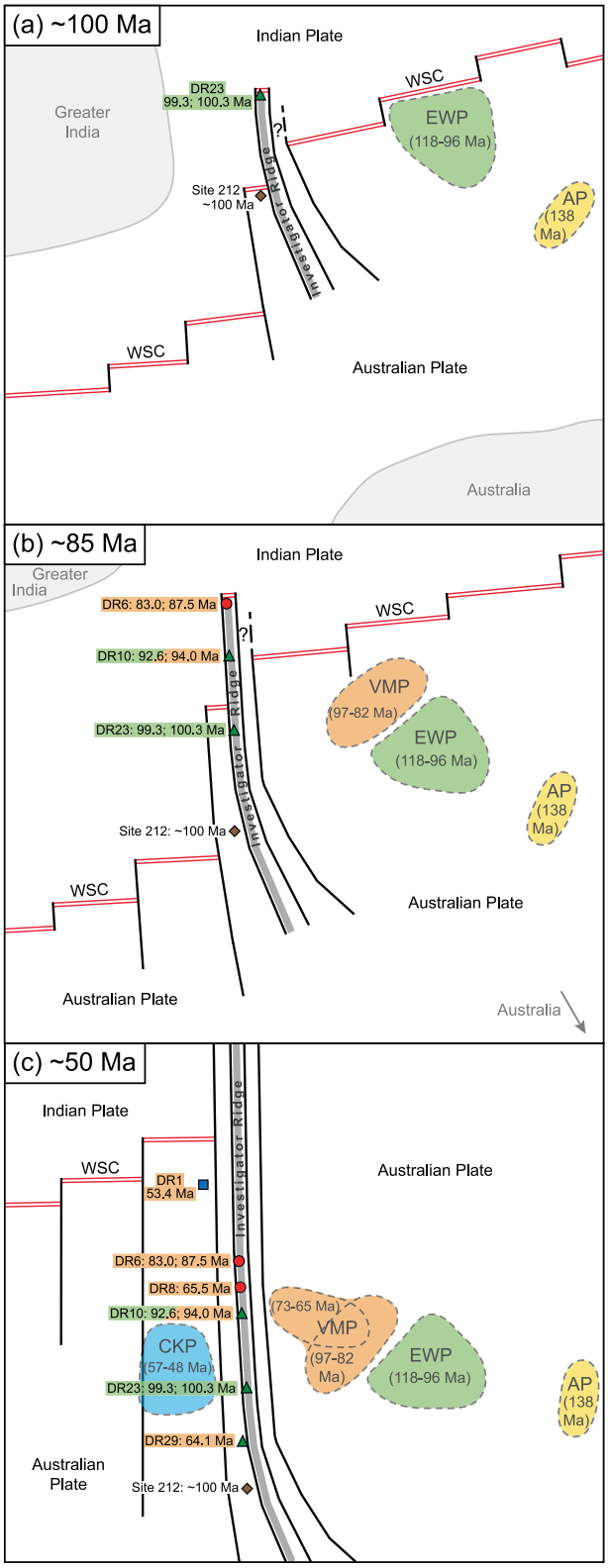

The correlation of isotope ratios with the $^{40}Ar/^{39}Ar$ ages suggests systematic compositional changes of the mantle source region with time and therefore a temporal geochemical evolution of the Indian Mantle Domain in the Eastern Indian Ocean, documented by the CHRISP and Investigator Ridge magmatism over a large time span between 138.4 Ma (and thus shortly after breakup of Gondwana) and 47.5 Ma. The mantle domain continuously evolved from being more depleted in terms of incompatible trace elements and with low $^{206}Pb/^{204}Pb$ ratios to more enriched in terms of incompatible trace elements with high $^{206}Pb/^{204}Pb$ ratios that contain higher proportions of a "C" or "FOZO" component but lower proportions of the SCLM material. The large range in $^{208}Pb/^{204}Pb$, $^{207}Pb/^{204}Pb$, Nd, Hf and Sr isotope ratios, especially observed in the CHRISP provinces, implies that the SCLM material was present in the Indian upper mantle in varying portions leading to variable mixing with the surrounding upper mantle material and heterogeneities in the Indian Mantle Domain. Interestingly, the plutonic samples from the Investigator Ridge overlap with or trend toward the Pliocene rocks from Christmas Island (UVS) on initial $^{206}Pb/^{204}Pb$ versus $^{208}Pb/^{204}Pb$ and $^{207}Pb/^{204}Pb$ diagrams and in Nd-Hf isotope space (Fig. 5b and 6a-b). This 5.1–3.1 Ma old magmatism represents a rejuvenated volcanic phase on the island and does not fit into the general trend of an increasing proportion of an enriched "C" or "FOZO" component in younger rocks. Instead, the melts from the UVS seem to have tapped parts of the mantle that preserved a higher portion of recycled SCLM material, otherwise mainly found in the older (~100 Ma) CHRISP rocks, showing that this material is still present in the Indian upper mantle and can be occasionally sampled (Hoernle et al., 2011a). Furthermore, on the εNd_i versus εHf_i diagram where the Investigator Ridge plutonic samples plot subparallel to the volcanic samples and the fields for the CHRISP sub-provinces including the Christmas Island LVS, they extend in the direction of the UVS samples that also deviate from the general trend of the CHRISP provinces, clearly plotting above both the Hf-Nd mantle array and the SWIR 39-41°S field (Fig. 5b). Therefore, both the Investigator Ridge plutonic and the UVS samples seem to be derived from a source with slightly more radiogenic Hf isotope compositions than the source containing SCLM material, which is preserved in the sampled rocks from the CHRISP and Investigator Ridge area. This observation further demonstrates that small-scale heterogeneities are present within the Indian upper mantle both geographically and temporally.

5. Conclusions

1) New $^{40}Ar/^{39}Ar$ ages of magmatic rocks from the Investigator Ridge decrease from 100.0 Ma to 83.0 Ma northward along the ridge, consistent with their formation at the WSC. The radiometric

Fig. 9. Simplified illustration of the formation history of the Investigator Ridge and the CHRISP volcanic sub-provinces between 100 Ma and 50 Ma. **(a)** The ~ 100 Ma old part of the Investigator Ridge (sample DR23) formed at the WSC±contemporaneously to the EWP. **(b)** At ~ 85 Ma ago, the rocks from DR6 formed at the spreading center, when the older part of the VMP was emplaced near the WSC. Samples from DR10 formed ~ 9 Ma earlier, when the youngest part of the EWP was emplaced and the earliest volcanic activity of the VMP started. **(c)** At ~ 50 Ma, CHRISP volcanism had already passed over the Investigator FZ system, including the emplacement of the younger VMP and DR8 and DR29 samples on and in the vicinity of the Investigator Ridge along with the first activity of the CKP and formation of the near-ridge Outsider Seamount. The colors of the denotation of the Investigator Ridge samples indicate their geochemical and geochronological similarity to the respective CHRISP sub-provinces (green = EWP, orange = VMP). The symbols for the dredge locations are the same as in the previous figures.

ages cover nearly half the duration of the Cretaceous Magnetic Quiet Zone and ground truth that the WSC became active significantly earlier than constrained by magnetic chrons thus far (C34; ~84 Ma Jacob et al., 2014; Liu et al., 1983). The Investigator Ridge represents a transverse ridge located directly east of one of several large FZs that make up the complex Investigator FZ system. The Investigator Ridge likely formed by tectonic uplift of crustal and upper mantle blocks in the framework of major plate reorganizations in the Eastern Indian Ocean and is possibly supported by current intraplate deformation along the N-S striking FZ fabrics.

2) Our new $^{40}Ar/^{39}Ar$ ages provide new insights into the crustal ages and displacements within the Investigator FZ because magnetic lineations have not been identified so far within the narrow strips between the individual fault zones. The new ages indicate that, in contrast to the so far exclusively observed left-lateral spreading axis offsets in the Wharton Basin, a large right-lateral offset of ~ 450 km could exist between the Investigator Ridge and the eastward lying crust of compartment H. Such dextral offsets could account for the ~ 11 Ma age difference between our $^{40}Ar/^{39}Ar$ ages and compartment H chrons. To the west, a ~ 1,200–1,300 km left-lateral ridge axis offset is required to correlate the chrons and is several hundred kilometers longer than previously estimated. About half of the offset most likely was compensated by a second FZ~30–50 km to the west of the Investigator Ridge. A few younger samples deviate from the observed age progressive trend and are geochemically more enriched than the Investigator Ridge MORB type rocks. They appear to be related to the CHRISP volcanism, which occurred at 72.8–47.5 Ma in the vicinity of the Investigator FZ and crossed the FZ in an E-W direction.

3) The radiogenic isotope compositions of the volcanic rocks from the Investigator Ridge display DUPAL-like compositions, similar to present-day Indian MORB. Isotope correlations imply mixing of an enriched common "C" or "FOZO" type component and a depleted DM type component admixed with an EMI type component. The Investigator Ridge plutonic rocks deviate from these mixing relations and require an additional component similar to recycled SCLM material proposed for the CHRISP. The restriction of SCLM isotopic flavors to intrusions could reflect smaller degrees of melting along an off-axis melt column. Correlations of our new $^{40}Ar/^{39}Ar$ ages with trace element and radiogenic isotope compositions for the Investigator Ridge and CHRISP samples suggest a relatively continuous evolution of the regional mantle. Compositions with low $^{206}Pb/^{204}Pb$ but more enriched $^{208}Pb/^{204}Pb$, $^{207}Pb/^{204}Pb$, Nd, Hf and Sr isotope flavors are observed for the ~ 120–90 Ma interval and changed to compositions dominated by a common "C" or "FOZO" component with high $^{206}Pb/^{204}Pb$ ratios ~ 40–50 M a ago.

CRediT authorship contribution statement

Antje Dürkefälden: Writing – original draft, Methodology, Formal analysis, Conceptualization. **Folkmar Hauff:** Writing – review & editing, Investigation, Funding acquisition, Conceptualization. **Kaj Hoernle:** Writing – review & editing, Investigation, Funding acquisition. **Maxim Portnyagin:** Writing – review & editing, Investigation. **Jo-Anne Wartho:** Writing – review & editing, Formal analysis. **Dieter Garbe-Schönberg:** Investigation. **Andrey Gurenko:** Investigation. **Paul van den Bogaard:** Investigation. **Andrea Kipf:** Investigation. **Marcus Gutjahr:** Investigation.

Declaration of competing interest

The authors declare that they have no known competing financial interests or personal relationships that could have appeared to influence the work reported in this paper.

Acknowledgements

We would like to thank Captain Mallon and his crew of the R/V SONNE for their support on board. U. Westernströer, Jan Sticklus and Silke Hauff are thanked for their analytical support and GEOMAR Helmholtz Centre Ocean Research Kiel for partial funding of the analytical work. Editorial handling by Prof. Sanghoon Kwon is much appreciated and two anonymous reviews helped to improve an earlier version. This study was supported by the German Ministry of Education and Research (BMBF) through grant number 03G0274A to K. Hoernle, F. Hauff and R. Werner. We dedicate this paper to our late colleague and friend Reinhard Werner whose expertise and enthusiasm exploring the mysteries of the deep ocean are greatly missed.

Appendix A. Supplementary data

Supplementary data to this article can be found online at https://doi.org/10.1016/j.gr.2024.07.016.

References

Baksi, A.K., 2007. A quantitative tool for detecting alteration in undisturbed rocks and minerals—I: Water, chemical weathering, and atmospheric argon, in Foulger, G.R., and Jurdy, D.M., eds., Plates, plumes, and planetary processes. Geol. Soc. Am. Spec. Pap. 430, 285–303. https://doi.org/10.1130/2007.2430(15).

Bonatti, E., 1978. Vertical tectonism in oceanic fracture zones. Earth Planet. Sc. Lett. 37, 369–379. https://doi.org/10.1016/0012-821X(78)90052-3.

Castillo, P., 1988. The Dupal anomaly as a trace of the upwelling lower mantle. Nature 336, 667–670. https://doi.org/10.1038/336667a0.

Chakrabarti, R., Basu, A.R., Paul, D.K., 2007. Nd–Hf–Sr–Pb isotopes and trace element geochemistry of Proterozoic lamproites from southern India: Subducted komatiite in the source. Chem. Geol. 236, 291–302. https://doi.org/10.1016/j.chemgeo.2006.10.006.

Connelly, J.N., Ulfbeck, D.G., Thrane, K., Bizzarro, M., Housh, T., 2006. A method for purifying Lu and Hf for analyses by MC-ICP-MS using TODGA resin. Chem. Geol. 233, 126–136. https://doi.org/10.1016/j.chemgeo.2006.02.020.

Deplus, C., 2001. Indian Ocean Actively Deforms. Science 292, 1850–1851. https://doi.org/10.1126/science.1061082.

Deplus, C., Diament, M., Hébert, H., Bertrand, G., Dominguez, S., Dubois, J., Malod, J., Patriat, P., Pontoise, B., Sibilla, J.-J., 1998. Direct evidence of active deformation in the eastern Indian oceanic plate. Geology 26, 131–134. https://doi.org/10.1130/0091-7613(1998)026<0131:Deoadi>2.3.Co;2.

Dick, H.J.B., Schouten, H., Meyer, P.S., Gallo, D.G., Bergh, H.W., Tyce, R., Patriat, P., Johnson, K.T.M., Snow, J., Fisher, A.T., 1991. Tectonic Evolution of the Atlantis II Fracture Zone. Proc. ODP Sc. Res. 118, 359–398.

Dixon, J.E., Leist, L., Langmuir, C., Schilling, J.-G., 2002. Recycled dehydrated lithosphere observed in plume-influenced mid-ocean-ridge basalt. Nature 420, 385–389. https://doi.org/10.1038/nature01215.

Dixon, J.E., Bindeman, I.N., Kingsley, R.H., Simons, K.K., Le Roux, P.J., Hajewski, T.R., Swart, P., Langmuir, C.H., Ryan, J.G., Walowski, K.J., Wada, I., Wallace, P.J., 2017. Light Stable Isotopic Compositions of Enriched Mantle Sources: Resolving the Dehydration Paradox. Geochem. Geophys. Geosyst. 18, 3801–3839. https://doi.org/10.1002/2016GC006743.

Dupré, B., Allègre, C.J., 1983. Pb-Sr isotope variation in Indian Ocean basalts and mixing phenomena. Nature 303, 142–146. https://doi.org/10.1038/303142a0.

Duputel, Z., Kanamori, H., Tsai, V.C., Rivera, L., Meng, L., Ampuero, J.-P., Stock, J.M., 2012. The 2012 Sumatra great earthquake sequence. Earth Planet. Sc. Lett. 351–352, 247–257. https://doi.org/10.1016/j.epsl.2012.07.017.

Escrig, S., Capmas, F., Dupre, B., Allegre, C.J., 2004. Osmium isotopic constraints on the nature of the DUPAL anomaly from Indian mid-ocean-ridge basalts. Nature 431, 59–63. https://doi.org/10.1038/nature02904.

Falloon, T.J., Hoernle, K., Schaefer, B.F., Bindeman, I.N., Hart, S.R., Garbe-Schonberg, D., Duncan, R.A., 2022. Petrogenesis of Lava from Christmas Island, Northeast Indian Ocean: Implications for the Nature of Recycled Components in Non-Plume Intraplate Settings. Geosciences 12, 118. https://doi.org/10.3390/geosciences12030118.

Fleck, R.J., Calvert, A.T., Coble, M.A., Wooden, J.L., Hodges, K., Hayden, L.A., van Soest, M.C., du Bray, E.A., John, D.A., 2019. Characterization of the rhyolite of Bodie Hills and $^{40}Ar/^{39}Ar$ intercalibration with Ar mineral standards. Chem. Geol. 525, 282–302. https://doi.org/10.1016/j.chemgeo.2019.07.022.

Fourny, A., Weis, D., Scoates, J.S., 2016. Comprehensive Pb-Sr-Nd-Hf isotopic, trace element, and mineralogical characterization of mafic to ultramafic rock reference materials. Geochem. Geophys. Geosyst. 17, 739–773. https://doi.org/10.1002/2015GC006181.

Fraser, K.J., Hawkesworth, C.J., Erlank, A.J., Mitchell, R.H., Scott-Smith, B.H., 1985. Sr, Nd and Pb isotope and minor element geochemistry of lamproites and kimberlites. Earth Planet. Sc. Lett. 76, 57–70. https://doi.org/10.1016/0012-821X(85)90148-7.

Fricker, M.B., Kutscher, D., Aeschlimann, B., Frommer, J., Dietiker, R., Bettmer, J., Günther, D., 2011. High spatial resolution trace element analysis by LA-ICP-MS using a novel ablation cell for multiple or large samples. Int. J. Mass Spectr. 307, 39–45. https://doi.org/10.1016/j.ijms.2011.01.008.
Garbe-Schönberg, C.-D., 1993. Simultaneous Determination Of Thirty-Seven Trace Elements In Twenty-Eight International Rock Standards By ICP-MS. Geostand. Newsletter 17, 81–97. https://doi.org/10.1111/j.1751-908X.1993.tb00122.x.
Gasperini, L., Bonatti, E., Borsetti, A.M., Capotondi, L., Cipriani, A., Negri, A., 2017. Timing of transverse ridge uplift along the Vema transform (Central Atlantic). Mar. Geol. 385, 228–232. https://doi.org/10.1016/j.margeo.2017.01.008.
Gautheron, C., Moreira, M., Gerin, C., Tassan-Got, L., Bezos, A., Humler, E., 2015. Constraints on the DUPAL anomaly from helium isotope systematics in the Southwest Indian mid-ocean ridge basalts. Chem. Geol. 417, 163–172. https://doi.org/10.1016/j.chemgeo.2015.10.005.
Gibbons, A.D., Barckhausen, U., van den Bogaard, P., Hoernle, K., Werner, R., Whittaker, J.M., Müller, R.D., 2012. Constraining the Jurassic extent of Greater India: Tectonic evolution of the West Australian margin. Geochem. Geophys. Geosyst. 13. https://doi.org/10.1029/2011GC003919.
Gibbons, A.D., Whittaker, J.M., Müller, R.D., 2013. The breakup of East Gondwana: Assimilating constraints from Cretaceous ocean basins around India into a best-fit tectonic model. J. Geophys. Res: Sol. Earth 118, 808–822. https://doi.org/10.1002/jgrb.50079.
Gordon, R.G., DeMets, C., Argus, D.F., 1990. Kinematic constraints on distributed lithospheric deformation in the equatorial Indian Ocean from present motion between the Australian and Indian Plates. Tectonics 9, 409–422. https://doi.org/10.1029/TC009i003p00409.
Govindaraju, K., 1994. 1994 Compilation of working values and sample description for 383 geostandards. Geostand. Newslett. 18, 1–158. https://doi.org/10.1046/j.1365-2494.1998.53202081.x-i1.
Grevemeyer, I., Rüpke, L.H., Morgan, J.P., Iyer, K., Devey, C.W., 2021. Extensional tectonics and two-stage crustal accretion at oceanic transform faults. Nature 591, 402–407. https://doi.org/10.1038/s41586-021-03278-9.
Griffin, W., Powell, W., Pearson, N., O'Reilly, S., 2008. GLITTER: data reduction software for laser ablation ICP-MS. Laser Ablation-ICP-MS in the Earth Sciences. Min. Assoc. of Can. Short Course Ser. 40, 204–207.
Hanan, B.B., Blichert-Toft, J., Pyle, D.G., Christie, D.M., 2004. Contrasting origins of the upper mantle revealed by hafnium and lead isotopes from the Southeast Indian Ridge. Nature 432, 91–94. https://doi.org/10.1038/nature03026.
Hanan, B.B., Graham, D.W., 1996. Lead and Helium Isotope Evidence from Oceanic Basalts for a Common Deep Source of Mantle Plumes. Science 272, 991–995. https://doi.org/10.1126/science.272.5264.991.
Hart, S.R., 1984. A large-scale isotope anomaly in the Southern Hemisphere mantle. Nature 309, 753–757. https://doi.org/10.1038/309753a0.
Hart, S.R., Hauri, E.H., Oschmann, L.A., Whitehead, J.A., 1992. Mantle Plumes and Entrainment: Isotopic Evidence. Science 256, 517–520. https://doi.org/10.1126/science.256.5056.517.
Hauri, E.H., Whitehead, J.A., Hart, S.R., 1994. Fluid dynamic and geochemical aspects of entrainment in mantle plumes. J. Geophys. Res: Sol. Earth 99, 24275–24300. https://doi.org/10.1029/94jb01257.
Heath, M., Phillips, D., Matchan, E.L., 2018. An evidence-based approach to accurate interpretation of $^{40}Ar/^{39}Ar$ ages from basaltic rocks. Earth Planet. Sc. Lett. 498, 65–76. https://doi.org/10.1016/j.epsl.2018.06.024.
Hoernle, K., Abt, D.L., Fischer, K.M., Nichols, H., Hauff, F., Abers, G.A., van den Bogaard, P., Heydolph, K., Alvarado, G., Protti, M., Strauch, W., 2008. Arc-parallel flow in the mantle wedge beneath Costa Rica and Nicaragua. Nature 451, 1094–1097. https://doi.org/10.1038/nature06550.
Hoernle, K., Hauff, F., Werner, R., van den Bogaard, P., Gibbons, A.D., Conrad, S., Muller, R.D., 2011a. Origin of Indian Ocean Seamount Province by shallow recycling of continental lithosphere. Nature Geosci. 4, 883–887. https://doi.org/10.1038/ngeo1331.
Hoernle, K., Hauff, F., Kokfelt, T.F., Haase, K., Garbe-Schönberg, D., Werner, R., 2011b. On- and off-axis chemical heterogeneities along the South Atlantic Mid-Ocean-Ridge (5–11°S): Shallow or deep recycling of ocean crust and/or intraplate volcanism? Earth Planet. Sc. Lett. 306, 86–97. https://doi.org/10.1016/j.epsl.2011.03.032.
Hofmann, A.W., 1988. Chemical differentiation of the Earth: the relationship between mantle, continental crust, and oceanic crust. Earth Planet. Sc. Lett. 90, 297–314. https://doi.org/10.1016/0012-821X(88)90132-X.
Jacob, J., Dyment, J., Yatheesh, V., 2014. Revisiting the structure, age, and evolution of the Wharton Basin to better understand subduction under Indonesia. J. Geophys. Res: Sol. Earth. 119, 169–190. https://doi.org/10.1002/2013JB010285.
Jarosewich, E., Nelen, J.A., Norberg, J.A., 1980. Reference Samples for Electron Microprobe Analysis. Geostand. Newslett. 4, 43–47. https://doi.org/10.1111/j.1751-908X.1980.tb00273.x.
Jochum, K.P., Verma, S.P., 1996. Extreme enrichment of Sb, Tl and other trace elements in altered MORB. Chem. Geol. 130, 289–299. https://doi.org/10.1016/0009-2541(96)00014-9.
Jochum, K.P., Nohl, U., Herwig, K., Lammel, E., Stoll, B., Hofmann, A.W., 2005. GeoReM: A New Geochemical Database for Reference Materials and Isotopic Standards. Geostand. Geoanal. Res. 29, 333–338. https://doi.org/10.1111/j.1751-908X.2005.tb00904.x.
Jochum, K.P., Stoll, B., Herwig, K., Willbold, M., Hofmann, A.W., Amini, M., Aarburg, S., Abouchami, W., Hellebrand, E., Mocek, B., Raczek, I., Stracke, A., Alard, O., Bouman, C., Becker, S., Dücking, M., Brätz, H., Klemd, R., de Bruin, D., Canil, D., Cornell, D., de Hoog, C.-J., Dalpé, C., Danyushevsky, L., Eisenhauer, A., Gao, Y., Snow, J.E., Groschopf, N., Günther, D., Latkoczy, C., Guillong, M., Hauri, E.H., Höfer, H.E., Lahaye, Y., Horz, K., Jacob, D.E., Kasemann, S.A., Kent, A.J.R., Ludwig, T., Zack, T., Mason, P.R.D., Meixner, A., Rosner, M., Misawa, K., Nash, B.P., Pfänder, J., Premo, W.R., Sun, W.D., Tiepolo, M., Vannucci, R., Vennemann, T., Wayne, D., Woodhead, J.D., 2006. MPI-DING reference glasses for in situ microanalysis: New reference values for element concentrations and isotope ratios. Geochem. Geophys. Geosyst. 7. https://doi.org/10.1029/2005GC001060.
Jochum, K.P., Weis, U., Stoll, B., Kuzmin, D., Yang, Q., Raczek, I., Jacob, D.E., Stracke, A., Birbaum, K., Frick, D.A., Günther, D., Enzweiler, J., 2011. Determination of Reference Values for NIST SRM 610–617 Glasses Following ISO Guidelines. Geostand. Geoanal. Res. 35, 397–429. https://doi.org/10.1111/j.1751-908X.2011.00120.x.
Jochum, K.P., Weis, U., Schwager, B., Stoll, B., Wilson, S.A., Haug, G.H., Andreae, M.O., Enzweiler, J., 2016. Reference Values Following ISO Guidelines for Frequently Requested Rock Reference Materials. Geostand. Geoanal. Res. 40, 333–350. https://doi.org/10.1111/j.1751-908X.2015.00392.x.
Jones, C.E., Jenkyns, H.C., 2001. Seawater strontium isotopes, oceanic anoxic events, and seafloor hydrothermal activity in the Jurassic and Cretaceous. Am. J. Sc. 301, 112–149. https://doi.org/10.2475/ajs.301.2.112.
Jourdan, F., Renne, P.R., Reimold, W.U., 2009. An appraisal of the ages of terrestrial impact structures. Earth Planet. Sc. Lett. 286, 1–13. https://doi.org/10.1016/j.epsl.2009.07.009.
Kempton, P.D., Pearce, J.A., Barry, T.L., Fitton, J.G., Langmuir, C., Christie, D.M., 2002. Sr-Nd-Pb-Hf Isotope Results from ODP Leg 187: Evidence for Mantle Dynamics of the Australian-Antarctic Discordance and Origin of the Indian MORB Source. Geochem. Geophys. Geosyst. 3, 1–35. https://doi.org/10.1029/2002GC000320.
Kendrick, M.A., Kamenetsky, V.S., Phillips, D., Honda, M., 2012. Halogen systematics (Cl, Br, I) in Mid-Ocean Ridge Basalts: A Macquarie Island case study. Geochim. Cosmochim. Ac. 81, 82–93. https://doi.org/10.1016/j.gca.2011.12.004.
Kendrick, M.A., Jackson, M.G., Kent, A.J.R., Hauri, E.H., Wallace, P.J., Woodhead, J., 2014. Contrasting behaviours of CO_2, S, H_2O and halogens (F, Cl, Br, and I) in enriched-mantle melts from Pitcairn and Society seamounts. Chem. Geol. 370, 69–81. https://doi.org/10.1016/j.chemgeo.2014.01.019.
Korsch, M.J., Gulson, B.L., 1986. Nd and Pb isotopic studies of an Archaean layered mafic-ultramafic complex, Western Australia, and implications for mantle heterogeneity. Geochim. Cosmochim. Ac. 50, 1–10. https://doi.org/10.1016/0016-7037(86)90042-6.
Lay, T., Ye, L., Ammon, C.J., Dunham, A., Koper, K.D., 2016. The 2 March 2016 Wharton Basin Mw 7.8 earthquake: High stress drop north-south strike-slip rupture in the diffuse oceanic deformation zone between the Indian and Australian Plates. Geophys. Res. Lett. 43, 7937–7945. https://doi.org/10.1002/2016GL069931.
Le Bas, M.J., Le Maitre, R.W., Streckeisen, A., Zanettin, B., Subcommission, I.U.G.S., on the Systematics of Igneous Rocks, 1986. A Chemical Classification of Volcanic Rocks Based on the Total Alkali-Silica Diagram. J. Petrol. 27, 745–750. https://doi.org/10.1093/petrology/27.3.745.
Le Voyer, M., Cottrell, E., Kelley, K.A., Brounce, M., Hauri, E.H., 2015. The effect of primary versus secondary processes on the volatile content of MORB glasses: An example from the equatorial Mid-Atlantic Ridge (5°N–3°S). J. Geophys. Res: Sol. Earth. 120, 125–144. https://doi.org/10.1002/2014JB011160.
Le Voyer, M., Kelley, K.A., Cottrell, E., Hauri, E.H., 2017. Heterogeneity in mantle carbon content from CO_2-undersaturated basalts. Nat. Comm. 8, 14062. https://doi.org/10.1038/ncomms14062.
Le Voyer, M., Hauri, E.H., Cottrell, E., Kelley, K.A., Salters, V.J.M., Langmuir, C.H., Hilton, D.R., Barry, P.H., Füri, E., 2019. Carbon Fluxes and Primary Magma CO_2 Contents Along the Global Mid-Ocean Ridge System. Geochem. Geophys. Geosyst. 20, 1387–1424. https://doi.org/10.1029/2018GC007630.
Liu, C.-S., Curray, J.R., McDonald, J.M., 1983. New constraints on the tectonic evolution of the eastern Indian Ocean. Earth Planet. Sc. Lett. 65, 331–342. https://doi.org/10.1016/0012-821X(83)90171-1.
Ludwig, K.A., 2011. A geochronological toolkit for Microsoft Excel. Berkeley Geochron. Centre Spec. Pub. No. 4, available at www.bgc.org/isoplot. Last accessed 23rd June 2024.
MacDonald, G.A., Katsura, I., 1964. Chemical Composition of Hawaiian Lavas. J. Petrol. 5, 82–133. https://doi.org/10.1093/petrology/5.1.82.
Marjanović, M., Singh, S.C., Gregory, E.P.M., Grevemeyer, I., Growe, K., Wang, Z., Vaddineni, V., Laurencin, M., Carton, H., Gómez de la Peña, L., Filbrandt, C., 2020. Seismic Crustal Structure and Morphotectonic Features Associated With the Chain Fracture Zone and Their Role in the Evolution of the Equatorial Atlantic Region. J. Geophys. Res: Sol. Earth 125, e2020JB020275. https://doi.org/10.1029/2020JB020275.
Meyzen, C.M., Ludden, J.N., Humler, E., Luais, B., Toplis, M.J., Mével, C., Storey, M., 2005. New insights into the origin and distribution of the DUPAL isotope anomaly in the Indian Ocean mantle from MORB of the Southwest Indian Ridge. Geochem. Geophys. Geosyst. 6, Q11K11. https://doi.org/10.1029/2005GC000979.
Michael, P.J., Schilling, J.-G., 1989. Chlorine in mid-ocean ridge magmas: Evidence for assimilation of seawater-influenced components. Geochim. Cosmochim. Ac. 53, 3131–3143. https://doi.org/10.1016/0016-7037(89)90094-X.
Muller, M.R., Minshull, T.A., White, R.S., 2000. Crustal structure of the Southwest Indian Ridge at the Atlantis II Fracture Zone. J. Geophys. Res: Sol. Earth 105, 25809–25828. https://doi.org/10.1029/2000JB900262.
Müller, R.D., Zahirovic, S., Williams, S.E., Cannon, J., Seton, M., Bower, D.J., Tetley, M.G., Heine, C., Le Breton, E., Liu, S., Russell, S.H.J., Yang, T., Leonard, J., Gurnis, M., 2019. A Global Plate Model Including Lithospheric Deformation Along Major Rifts and Orogens Since the Triassic. Tectonics 38, 1884–1907. https://doi.org/10.1029/2018tc005462.

Murphy, D.T., Collerson, K.D., Kamber, B.S., 2002. Lamproites from Gaussberg, Antarctica: Possible Transition Zone Melts of Archaean Subducted Sediments. J. Petrol. 43, 981–1001. https://doi.org/10.1093/petrology/43.6.981.

Nelson, D.R., McCulloch, M.T., Sun, S.-S., 1986. The origins of ultrapotassic rocks as inferred from Sr, Nd and Pb isotopes. Geochim. Cosmochim. Ac. 50, 231–245. https://doi.org/10.1016/0016-7037(86)90172-9.

Newman, S., Lowenstern, J.B., 2002. VolatileCalc: a silicate melt–H_2O–CO_2 solution model written in Visual Basic for excel. Comp. Geosc. 28, 597–604. https://doi.org/10.1016/S0098-3004(01)00081-4.

Pearce, J.A., 2008. Geochemical fingerprinting of oceanic basalts with applications to ophiolite classification and the search for Archean oceanic crust. Lithos 100, 14–48. https://doi.org/10.1016/j.lithos.2007.06.016.

Pearce, J.A. 1996. A User's Guide to Basalt Discrimination Diagrams. In: Wyman, D. A., Ed., Trace Element Geochemistry of Volcanic Rocks: Applications for Massive Sulphide Exploration. Geol. Assoc. Can., Short Course Notes 12, 79-113.

Pettke, T., Halter, W.E., Webster, J.D., Aigner-Torres, M., Heinrich, C.A., 2004. Accurate quantification of melt inclusion chemistry by LA-ICPMS: a comparison with EMP and SIMS and advantages and possible limitations of these methods. Lithos 78, 333–361. https://doi.org/10.1016/j.lithos.2004.06.011.

Pockalny, R.A., Gente, P., Buck, R., 1996. Oceanic transverse ridges: A flexural response to fracture-zone–normal extension. Geology 24, 71–74. https://doi.org/10.1130/0091-7613(1996)024<0071:Otrafr>2.3.Co;2.

Portnyagin, M.V., Ponomareva, V.V., Zelenin, E.A., Bazanova, L.I., Pevzner, M.M., Plechova, A.A., Rogozin, A.N., Garbe-Schönberg, D., 2020. TephraKam: geochemical database of glass compositions in tephra and welded tuffs from the Kamchatka volcanic arc (northwestern Pacific). Earth Syst. Sci. Data 12, 469–486. https://doi.org/10.5194/essd-12-469-2020.

Rehkämper, M., Hofmann, A.W., 1997. Recycled ocean crust and sediment in Indian Ocean MORB. Earth Planet. Sc. Lett. 147, 93–106. https://doi.org/10.1016/S0012-821X(97)00009-5.

Royer, J.-Y., Gordon, R.G., 1997. The Motion and Boundary Between the Capricorn and Australian Plates. Science 277, 1268–1274. https://doi.org/10.1126/science.277.5330.1268.

Samrock, L.K., Wartho, J.-A., Hansteen, T.H., 2019. ^{40}Ar-^{39}Ar geochronology of the active phonolitic Cadamosto Seamount, Cape Verde. Lithos 344–345, 464–481. https://doi.org/10.1016/j.lithos.2019.07.003.

Sclater, J.G., Fisher, R.L., 1974. Evolution of the East-Central Indian Ocean, with Emphasis on the Tectonic Setting of the Ninetyeast Ridge. Geol. Soc. Am. Bull. 85, 683–702. https://doi.org/10.1130/0016-7606(1974)85<683:Eoteci>2.0.Co;2.

Seton, M., Müller, R.D., Zahirovic, S., Gaina, C., Torsvik, T., Shephard, G., Talsma, A., Gurnis, M., Turner, M., Maus, S., Chandler, M., 2012. Global continental and ocean basin reconstructions since 200Ma. Earth-Sci. Rev. 113, 212–270. https://doi.org/10.1016/j.earscirev.2012.03.002.

Sobolev, A.V., Asafov, E.V., Gurenko, A.A., Arndt, N.T., Batanova, V.G., Portnyagin, M. V., Garbe-Schönberg, D., Krasheninnikov, S.P., 2016. Komatiites reveal a hydrous Archaean deep-mantle reservoir. Nature 531, 628–632. https://doi.org/10.1038/nature17152.

Steiger, R.H., Jäger, E., 1977. Subcommission on geochronology: Convention on the use of decay constants in geo- and cosmochronology. Earth Planet. Sc. Lett. 36, 359–362. https://doi.org/10.1016/0012-821X(77)90060-7.

Storey, M., Saunders, A.D., Tarney, J., Gibson, I.L., Norry, M.J., Thirlwall, M.F., Leat, P., Thompson, R.N., Menzies, M.A., 1989. Contamination of Indian Ocean asthenosphere by the Kerguelen-Heard mantle plume. Nature 338, 574–576. https://doi.org/10.1038/338574a0.

Stracke, A., Bizimis, M., Salters, V.J.M., 2003. Recycling oceanic crust: Quantitative constraints. Geochem. Geophys. Geosyst. 4, 8003. https://doi.org/10.1029/2001gc000223.

Stracke, A., Hofmann, A.W., Hart, S.R., 2005. FOZO, HIMU, and the rest of the mantle zoo. Geochem. Geophys. Geosyst. 6, Q05007. https://doi.org/10.1029/2004gc000824.

Stroncik, N.A., Haase, K.M., 2004. Chlorine in oceanic intraplate basalts: Constraints on mantle sources and recycling processes. Geology 32, 945–948. https://doi.org/10.1130/g21027.1.

Sushchevskaya, N., Belyatsky, B., Tsekhonya, T., Mirlin, E.G., Nikulin, V.V., Romashova, T.V., Sedykh, E.M., 1998. Petrology and Geochemistry of Basalts from the Eastern Indian Ocean: Implications for its Early Evolution. Petrology 6, 480–505.

Sushchevskaya, N., Belyatsky, B., Nikulin, V., 2000. Geochemical heterogeneity of the magmatism from the Ninetyeast and Investigator Ridges, Goldschmidt Conference, Oxford UK. J. Conf. Abs. 5 (2), 968–969.

Taneja, R., Rushmer, T., Blichert-Toft, J., Turner, S., O'Neill, C., 2016. Mantle heterogeneities beneath the Northeast Indian Ocean as sampled by intraplate volcanism at Christmas Island. Lithos 262, 561–575. https://doi.org/10.1016/j.lithos.2016.07.027.

Todd, E., Stracke, A., Scherer, E.E., 2015. Effects of simple acid leaching of crushed and powdered geological materials on high-precision Pb isotope analyses. Geochem. Geophys. Geosyst. 16, 2276–2302. https://doi.org/10.1002/2015GC005804.

van den Bogaard, P., 2013. The origin of the Canary Island Seamount Province - New ages of old seamounts. Sc. Rep. 3, 2107. https://doi.org/10.1038/srep02107.

Verma, S.P., 1992. Seawater alteration effects on REE, K, Rb, Cs, Sr, U, Th, Pb and Sr–Nd–Pb isotope systematics of Mid-Ocean Ridge Basalt. Geochem. J. 26, 159–177. https://doi.org/10.2343/geochemj.26.159.

von der Borch, C.C., Sclater, J.G., Gartner, S., Hekinian, R., Johnson, D.A., McGowran, B., Pimm, A.C., Thompson, R.W., Veevers, J.J., Waterman, L.S., 1974. Site 212 Site Report, DSDP Volume 22. Part 1, 37–83. https://doi.org/10.2973/dsdp.proc.22.103.1974.

Wallace, P., Carmichael, I.S.E., 1992. Sulfur in basaltic magmas. Geochim. Cosmochim. Ac. 56, 1863–1874. https://doi.org/10.1016/0016-7037(92)90316-B.

Wallace, P.J., Edmonds, M., 2011. The Sulfur Budget in Magmas: Evidence from Melt Inclusions, Submarine Glasses, and Volcanic Gas Emissions. Rev. Min. Geochem. 73, 215–246. https://doi.org/10.2138/rmg.2011.73.8.

Wang, W., Kelley, K.A., Li, Z., Chu, F., Dong, Y., Chen, L., Dong, Y., Li, J., 2021. Volatile Element Evidence of Local MORB Mantle Heterogeneity Beneath the Southwest Indian Ridge, 48°–51°E. Geochem. Geophys. Geosyst. 22, e2021GC009647. https://doi.org/10.1029/2021GC009647.

Wen, L., 2006. A compositional anomaly at the Earth's core–mantle boundary as an anchor to the relatively slowly moving surface hotspots and as source to the DUPAL anomaly. Earth Planet. Sc. Lett. 246, 138–148. https://doi.org/10.1016/j.epsl.2006.04.024.

Werner, R., Hauff, F., Hoernle, K., 2009. Christmas Island Seamount Province and the Investigator Ridge: Age and Causes of Intraplate Volcanism and Geodynamic Evolution of the South-Eastern Indian Ocean. RV SONNE Fahrtbericht / Cruise Report SO199 CHRISP, 85 pp. dOI: 10.3289/ifm-geomar_rep_25_2009.

Willbold, M., Stracke, A., 2006. Trace element composition of mantle end-members: Implications for recycling of oceanic and upper and lower continental crust. Geochem. Geophys. Geosyst. 7, Q04004. https://doi.org/10.1029/2005gc001005.

Workman, R.K., Hart, S.R., 2005. Major and trace element composition of the depleted MORB mantle (DMM). Earth Planet. Sc. Lett. 231, 53–72. https://doi.org/10.1016/j.epsl.2004.12.005.